

Ariel II Engineering Data Analysis

Phase III (Final) Report

22 November 1965

Contract Number NAS5-9104

Prepared by

Westinghouse Electric Corporation

Aerospace Division

Baltimore, Maryland

for

Goddard Space Flight Center

Greenbelt, Maryland

ABSTRACT

23750

Final conclusions relating to the dynamical behavior and the power system performance of the Ariel II International Satellite are developed and summarized in this phase III report. The emphasis in phase III has been on causal factors for performance previously summarized in phase II on the basis of reduced telemetry data from phase I.

Aerodynamic torques are charged with the responsibility for the observed spin rate variations and final stoppage, and together with gravity gradient torques, for the deduced precession of the satellite spin axis.

An intermittent circuit malfunction in the inverter is regarded as the most likely cause of the data anomaly in orbit 415. Otherwise the power system is shown to have functioned within design specifications or to have surpassed them.

## TABLE OF CONTENTS

| <u>Section</u>  | <u>Page</u> |
|---|-------------|
| ABSTRACT. . . . .   | i           |
| 1.0 INTRODUCTION. . . . .                                   | 1           |
| 2.0 DYNAMICAL ANALYSIS. . . . .                             | 2           |
| 2.1 SPACECRAFT INERTIA DATA . . . . .                       | 2           |
| 2.2 SOLAR PADDLE GEOMETRY . . . . .                         | 3           |
| 2.3 SPIN AXIS TORQUES AND ACCELERATIONS . . . . .           | 9           |
| 2.3.1 EQUIVALENT AIR DENSITY. . . . .                       | 11          |
| 2.3.2 AERODYNAMIC FORCES. . . . .                           | 14          |
| 2.3.3 AERODYNAMIC SPIN TORQUES AND ACCELERATION . . . . .   | 18          |
| 2.3.4 SOLAR PRESSURE SPIN TORQUE AND ACCELERATION . . . . . | 23          |
| 2.4 SPACECRAFT ORIENTATION. . . . .                         | 24          |
| 2.4.1 VELOCITY ASPECT ANGLE . . . . .                       | 25          |
| 2.4.2 SPIN AXIS ORIENTATION . . . . .                       | 29          |
| 2.5 SPACECRAFT STABILITY. . . . .                           | 34          |
| 2.6 PRECESSION TORQUES. . . . .                             | 35          |
| 2.6.1 GRAVITY GRADIENT TORQUE . . . . .                     | 36          |
| 2.6.2 AERODYNAMIC PRECESSION TORQUE . . . . .               | 38          |
| 2.7 DYNAMICAL CONCLUSIONS AND RECOMMENDATIONS . . . . .     | 41          |
| 3.0 POWER SYSTEM PERFORMANCE. . . . .                       | 42          |
| 3.1 BATTERY PERFORMANCE . . . . .                           | 42          |
| 3.1.1 BATTERY TERMINAL VOLTAGE. . . . .                     | 43          |
| 3.1.2 BATTERY CHARGE EFFICIENCY . . . . .                   | 43          |
| 3.1.3 BATTERY TEMPERATURE . . . . .                         | 47          |
| 3.1.4 STANDBY BATTERY . . . . .                             | 47          |

TABLE OF CONTENTS (Continued)

| <u>Section</u> |   | <u>Page</u> |
|----------------|---|-------------|
| 3.2            | SOLAR PADDLES PERFORMANCE . . . . .             | 48          |
| 3.3            | REGULATORS. . . . .                             | 52          |
| 3.3.1          | BATTERY CHARGE AND PROTECTION CIRCUIT . . . . . | 52          |
| 3.3.2          | PLUS AND MINUS REGULATORS . . . . .             | 54          |
| 3.4            | POWER SYSTEM ANOMALIES. . . . .                 | 54          |
| 3.4.1          | ORBIT 415 ANOMALY . . . . .                     | 54          |
| 3.4.2          | ORBIT 704 ANOMALY . . . . .                     | 59          |
| 3.4.3          | INITIAL POWER LOSS ANOMALY. . . . .             | 60          |
| 3.5            | POWER SYSTEM CONCLUSIONS. . . . .               | 62          |

LIST OF FIGURES

| <u>Figure</u> |  | <u>Page</u> |
|---------------|--|-------------|
| 1             | VARIATION OF SPIN RATE WITH TIME. . . . .                                      | 10          |
| 2             | VARIATION OF SOLAR ASPECT ANGLE TIME. . . . .                                  | 12          |
| 3             | VARIATION OF SPIN ACCELERATION WITH TIME. . . . .                              | 26          |
| 4             | VARIATION OF ORIENTATION/VELOCITY ANGEL WITH TIME .                            | 28          |
| 5             | VARIATION OF ORIENTATION/VELOCITY ANGLE WITH TIME<br>BASED ON COS.COS. . . . . | 30          |
| 6             | SPACECRAFT ORIENTATION. . . . .  | 33          |
| 7             | ANGLE BETWEEN ORBIT VECTOR AND SPIN VECTOR. . . . .                            | 37          |
| 8             | VELOCITY ASPECT ANGLE, $\theta_v$ , DEG. . . . .                               | 40          |
| 9             | BATTERY TERMINAL VOLTAGE VS. BATTERY TEMPERATURE. .                            | 44          |
| 10            | SCATTER DIAGRAM OF CHARGE TIME VS. TIME . . . . .                              | 46          |
| 11            | SOLAR ASPECT ANGLE VS. EFFECTIVE PADDLE SIDES . . .                            | 49          |
| 12            | NORMALIZED SOLAR CURRENT VS. DAYS FROM LAUNCH . . .                            | 50          |
| 13            | SIMPLIFIED POWER SUPPLY SYSTEM DIAGRAM. . . . .                                | 53          |
| 14            | SOLAR PADDLE POWER VS. DAYS FROM LAUNCH . . . . .                              | 61          |

## 1.0 INTRODUCTION

The Ariel II post-launch evaluation pursued under this contract has had three distinct areas of interest, namely, dynamics, power system and thermal performance. The potentialities of the data were exhausted in the last area at the conclusion of phase II. Results showed that pre-launch predicted thermal performance was borne out reasonably well by the actual spacecraft in orbit. Final reporting is now made in the remaining areas.

In this phase III report, which is also the final report under the contract, an attempt is made to explain the performance summarized in the phase II report. Possible causes are identified for any unusual parameter variations.

All the work rests upon the data reduced to engineering units in phase I from the telemetered data received as printouts from GSFC and also from the United Kingdom. Use was also made of the orbital data presented in the Refined and Predicted World Maps. The phase I report, reference 1, explains the data reduction task and displays the results. Phase II resulted in a concise statement of the data, i.e., a declaration of just what the spacecraft performance was. These data were cast in terms suitable for comparison to pre-launch prediction where applicable.

Care has been taken, both in the phase II report and also in this one, to indicate the level of confidence which may be placed in the conclusions. Such care is necessary because much of the work is built up from inference and deduction with reliance on data of incidental relevance. This is particularly true in the dynamics area, though not confined there.

Nevertheless, certain facts may be stated, at least qualitatively, with firmness. For example, aerodynamic disturbance torques acting on the solar paddles are the most significant ones from the spin torque point of view and are also significant from the precession torque point of view. These firmer facts make themselves evident in the discussion.

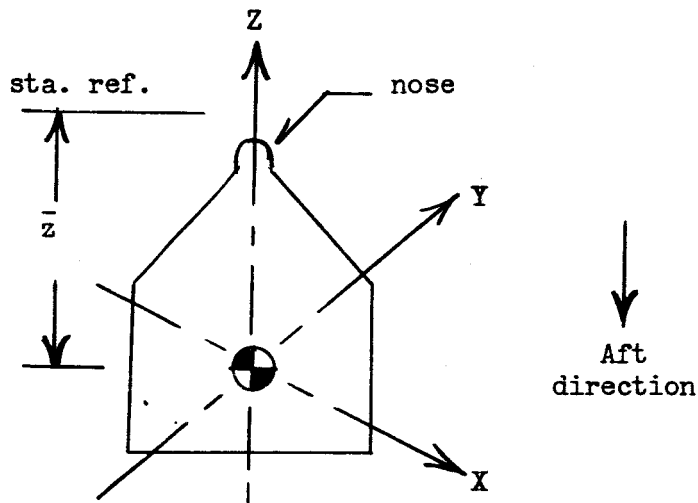
In general, the power system performed within predicted boundaries, with one seven-minute period of anomalous operation which has proved difficult to explain. Considerable effort has been devoted to examining available evidence and it appears that a good case can be developed for holding the inverter responsible. All of the chain of reasoning employed in these deductions is presented.

Conclusions and recommendations are stated separately in connection with each subject area because the conclusions themselves have no great inter-relationship. The dynamics question is considered first.

## 2.0 DYNAMICAL ANALYSIS

### 2.1 Spacecraft Inertia Data

The following inertia data for Ariel II is based on the orbital configuration of the satellite according to Outline Drawing 702R482, Rev. H. The orbital configuration has booms, paddles and antennas erected and deployed and includes the orbital portion of the separation mechanism.



|                | Mass moment of inertia |                   |
|----------------|------------------------|-------------------|
|                | slug-ft <sup>2</sup>   | Kg-m <sup>2</sup> |
| I <sub>x</sub> | 45.58                  | 61.79             |
| I <sub>y</sub> | 6.40                   | 8.68              |
| I <sub>z</sub> | 47.72                  | 64.70             |

$$(I = \text{slug-ft}^2 \times \frac{1}{0.7376} \frac{\text{Kg-m}^2}{\text{slug-ft}^2})$$

The center of mass of the satellite is:

$$\bar{x} \doteq 0 \quad (\text{measured from Z - axis})$$

$$\bar{y} \doteq 0 \quad (\text{measured from Z - axis})$$

$$\bar{z} = \text{sta } 36.14 \text{ in. (measured from station reference -- 8.630 in. ahead of nose)}$$

$$= \text{sta } 0.918 \text{ m}$$

## 2.2 Solar Paddle Geometry

The satellite has four solar paddles all with the same surface area. Opposite paddles have identical angular settings whereas adjacent paddles differ. Although each paddle actually has a double-wedge cross-section, it is assumed for convenience that each paddle is a flat plate.

From Outline Drawing 702R482, Rev. H, the paddle dimensions are obtained:

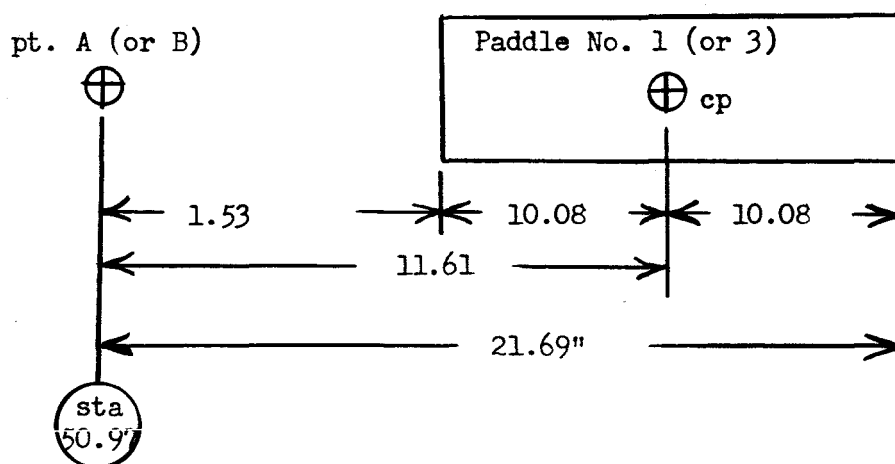
$$\text{length} = 20.16 \text{ in.}$$

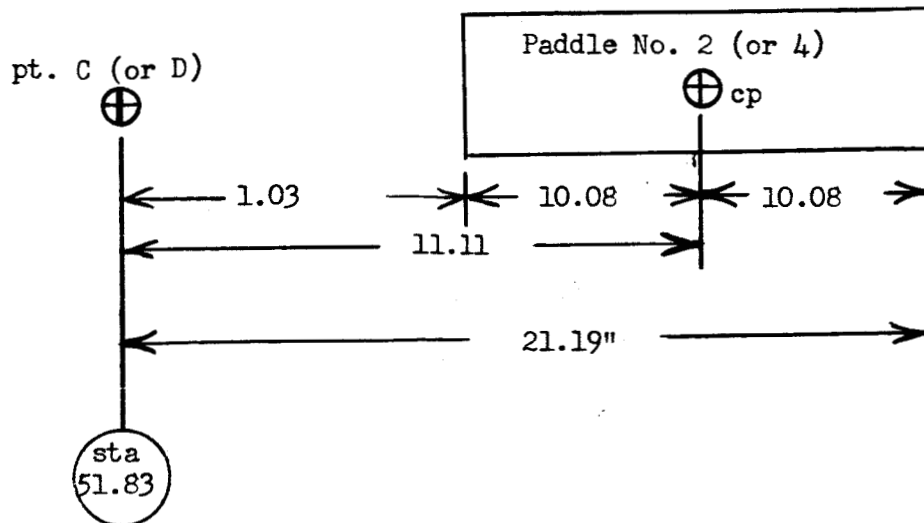
$$\text{width} = 11.98 \text{ in.}$$

The surface area of one side of one paddle is then:

$$\begin{aligned} S_1 &= 20.16 \times 11.98 \\ &= 241 \text{ in}^2 \\ &= 0.1555 \text{ m}^2 \end{aligned}$$

The normal view of each paddle itself is:





The above views give the true distances between the reference point and the center of pressure, cp, which is considered to be at the center of the paddle. The apparent distance between the reference point and the cp of each paddle as projected on the X-Y plane is:

$$l'_i = l_i \cos \alpha_i$$

where:

$$l_i = \text{true distance}$$

$$\alpha_i = \text{latitude of paddle shaft}$$

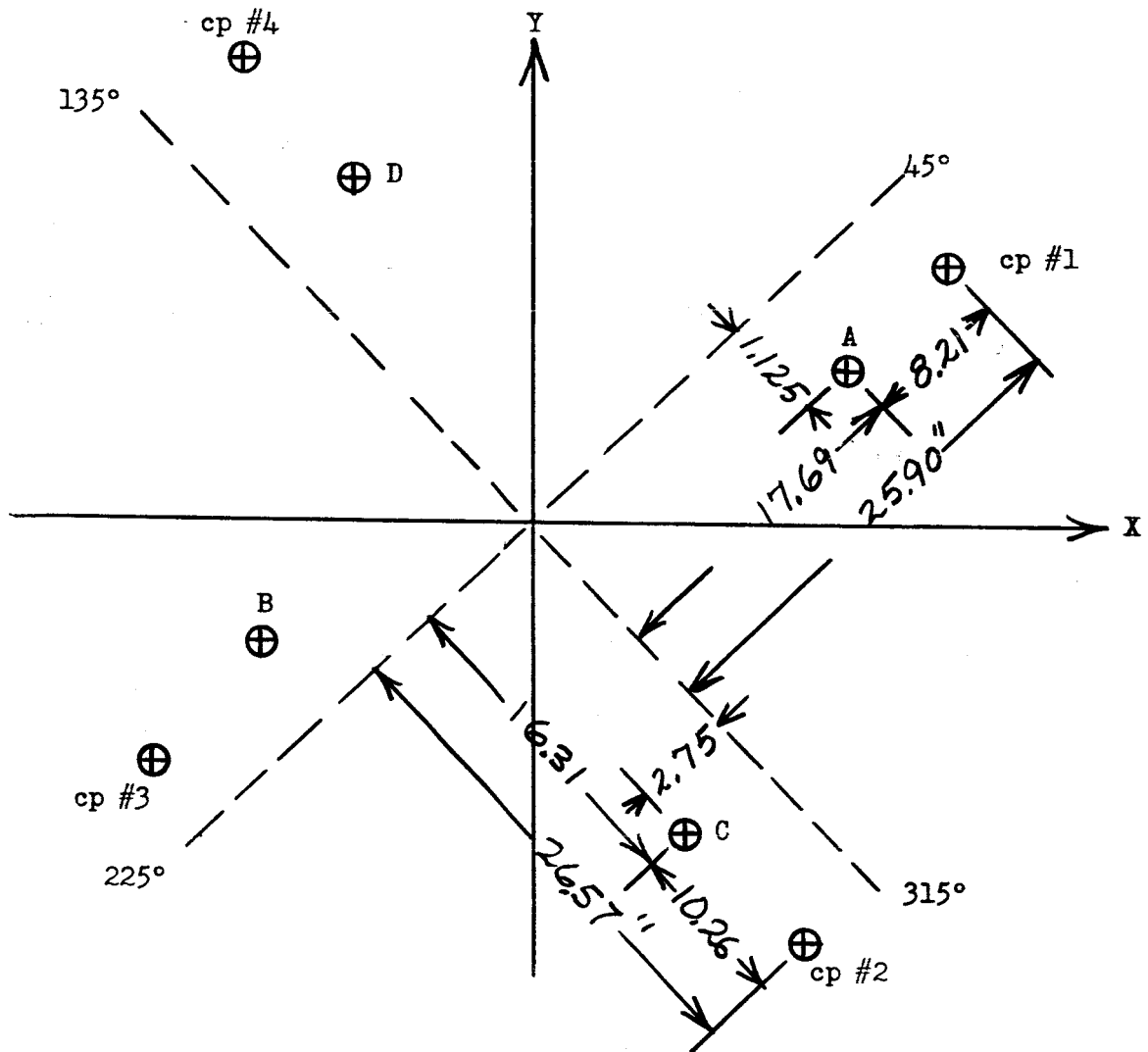
For paddle #1 (or 3):

$$\begin{aligned} l'_1 &= 11.61 \cos 45^\circ \\ &= \underline{8.21} \text{ in.} \end{aligned}$$

For paddle #2 (or 4):

$$\begin{aligned} l'_2 &= 11.11 \cos 22.5^\circ \\ &= \underline{10.26} \text{ in.} \end{aligned}$$

The apparent locations of reference points and cp's, as projected on the X-Y plane, are shown below in a plan view looking aft.



The cartesian coordinates of each cp are obtained trigonometrically:

For paddle #1:

$$\begin{aligned}
 x_1 &= (25.90 + 1.125) \cos 45^\circ \\
 &= \underline{17.67} \text{ in.}
 \end{aligned}$$

$$\begin{aligned}
 y_1 &= (25.90 - 1.125) \sin 45^\circ \\
 &= \underline{17.51} \text{ in.}
 \end{aligned}$$

$$\begin{aligned}
z_1 &= -\text{sta. } 50.97 - 11.61 \sin 45^\circ \\
&= -\text{sta. } 58.18 \text{ in (measured from station reference)} \\
&= -\text{sta. } 58.18 + \text{sta. } 36.14 \\
&= \underline{-22.02} \text{ in. (from center of mass)}.
\end{aligned}$$

For paddle #2:

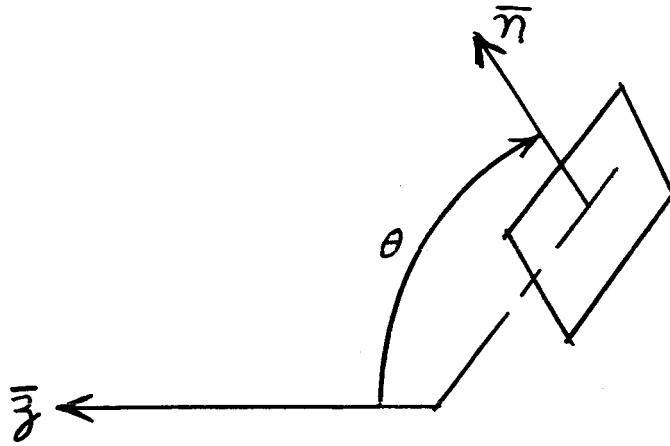
$$\begin{aligned}
x_2 &= (26.57 - 2.75) \cos 45^\circ \\
&= \underline{16.82} \text{ in.} \\
y_2 &= -(26.57 + 2.75) \sin 45^\circ \\
&= \underline{-20.7} \text{ in.} \\
z_2 &= -\text{sta. } 51.83 - 11.11 \sin 22.5^\circ \\
&= -\text{sta. } 56.08 \text{ in.} \\
&= -\text{sta. } 56.08 + \text{sta. } 36.14 \\
&= \underline{-19.94} \text{ in. (from center of mass)}
\end{aligned}$$

The coordinates of the cp for each paddle relative to the center of mass of the satellite are tabulated below:

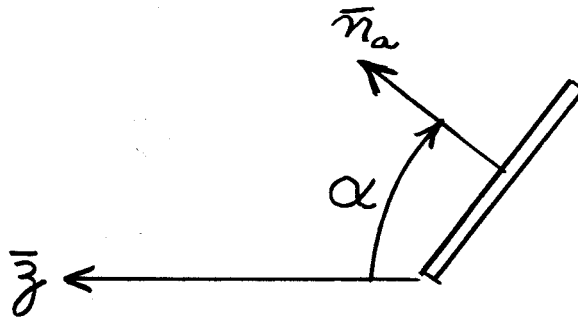
| Paddle<br>No. | cp Coordinates (in.) |        |        |
|---------------|----------------------|--------|--------|
|               | x                    | y      | z      |
| 1             | 17.67                | 17.51  | -22.02 |
| 2             | 16.82                | -20.7  | -19.94 |
| 3             | -17.67               | -17.51 | -22.02 |
| 4             | -16.82               | 20.7   | -19.94 |

To determine the angular orientation of the solar paddles:

a. Let  $\theta$  be the angle between the satellite spin axis,  $z$ , and the paddle normal,  $n$ , in the plane containing  $z$  and  $n$ .



b. Let  $\alpha$  be the angle between the spin axis,  $z$ , and the normal of the paddle axis,  $n_a$ , in the plane which includes the spin axis and the paddle axis.



c. Let  $\beta$  be the angle between the above normal of the paddle axis,  $n_a$ , and the normal of the paddle,  $n$ , i.e., paddle rotation. The angle,  $\theta$ , may be determined from the relation:

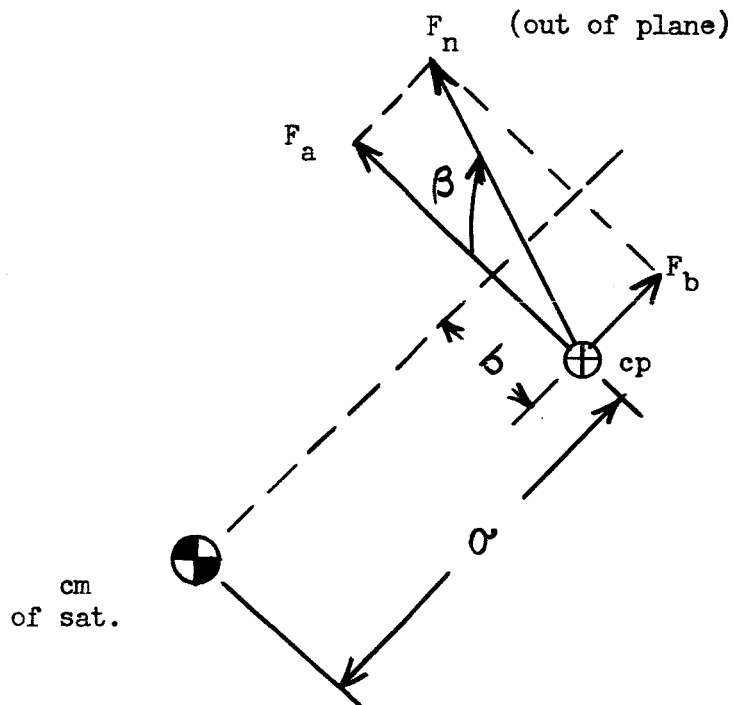
$$\cos \theta = \cos \alpha \cos \beta$$

The paddle orientation angles are:

| Paddle No. | Angle (deg) |         |          |
|------------|-------------|---------|----------|
|            | $\alpha$    | $\beta$ | $\theta$ |
| 1,3        | 45          | 57      | 67.4     |
| 2,4        | 22.5        | 57      | 59.8     |

It will prove useful to develop expressions for torques about the spin axis caused by forces normal to the paddles acting through the paddle centers of pressure.

A typical paddle projection showing the out-of-plane normal force,  $F_n$ , is constructed below:



The normal force may be resolved into:  $F_a = F_n \sin \beta$   
 $F_b = F_n \sin \alpha \cos \beta$

The general torque equation is:

$$\bar{T} = \bar{r} \times \bar{F}$$

The torque about the spin axis, z, of the satellite is for any one paddle:

$$\begin{aligned} T_{zi} &= a F_a + b F_b \\ &= (a \sin \beta + b \sin \alpha \cos \beta) F_{ni} \\ &= c_i F_{ni} \end{aligned}$$

It is seen that while  $F_{ni}$  might be a function of a number of variables including the angle of incidence, the part within parenthesis ( $c_i$ ) is a function of geometry only and is independent of other variables. Solving for the value of  $c_i$  for each paddle:

| Symbol   | Units | Paddle No. |        |
|--|-------|------------|--------|
|  |       | 1 or 3     | 2 or 4 |
| b  | in.   | 1.125      | 2.75   |
| a  | in.   | 25.90      | 26.97  |
| $\alpha$                                       | deg.  | 45         | 22.5   |
| $\beta$  | deg.  | 57         | 57     |
| $a \sin \beta$                                 | in.   | 21.7       | 22.3   |
| $b \sin \alpha \cos \beta$                     | in.   | 0.433      | 0.573  |
| $c = a \sin \alpha + b \sin \alpha \cos \beta$ | in.   | 22.1       | 22.9   |
|  | m     | 0.561      | 0.582  |

The torque about the spin axis for all four paddles is:

$$\begin{aligned}
 T_z &= \sum_i T_{zi} \\
 &= 2c_1 F_{n1} + 2c_2 F_{n2} \\
 &= 2 \times 0.561 F_{n1} + 2 \times 0.582 F_{n2} \\
 T_z &= 1.122 F_{n1} + 1.164 F_{n2} \text{ (nt-m)}
 \end{aligned}$$

### 2.3 Spin Axis Torques and Accelerations

The spin rate characteristic of Ariel II is an item of primary interest because the satellite did not perform as anticipated. The measured spin rate curve of Figure 1 illustrates how the spacecraft failed to maintain a steady spin rate as expected but instead decreased rapidly from an initial spin rate of 5.6 rpm down to 2.2 rpm then increased to 3 rpm. After two more spin reversal cycles the satellite stopped spinning entirely about 190 days after launch. The origin of Figure 1 is explained in references 1 and 2.

Since the spinning action of the spacecraft is essential to its successful operation, an explanation of the actual spin rate behavior of the satellite is of particular concern.

Torques about the spin axis which might explain Ariel II's spin rate behavior include:

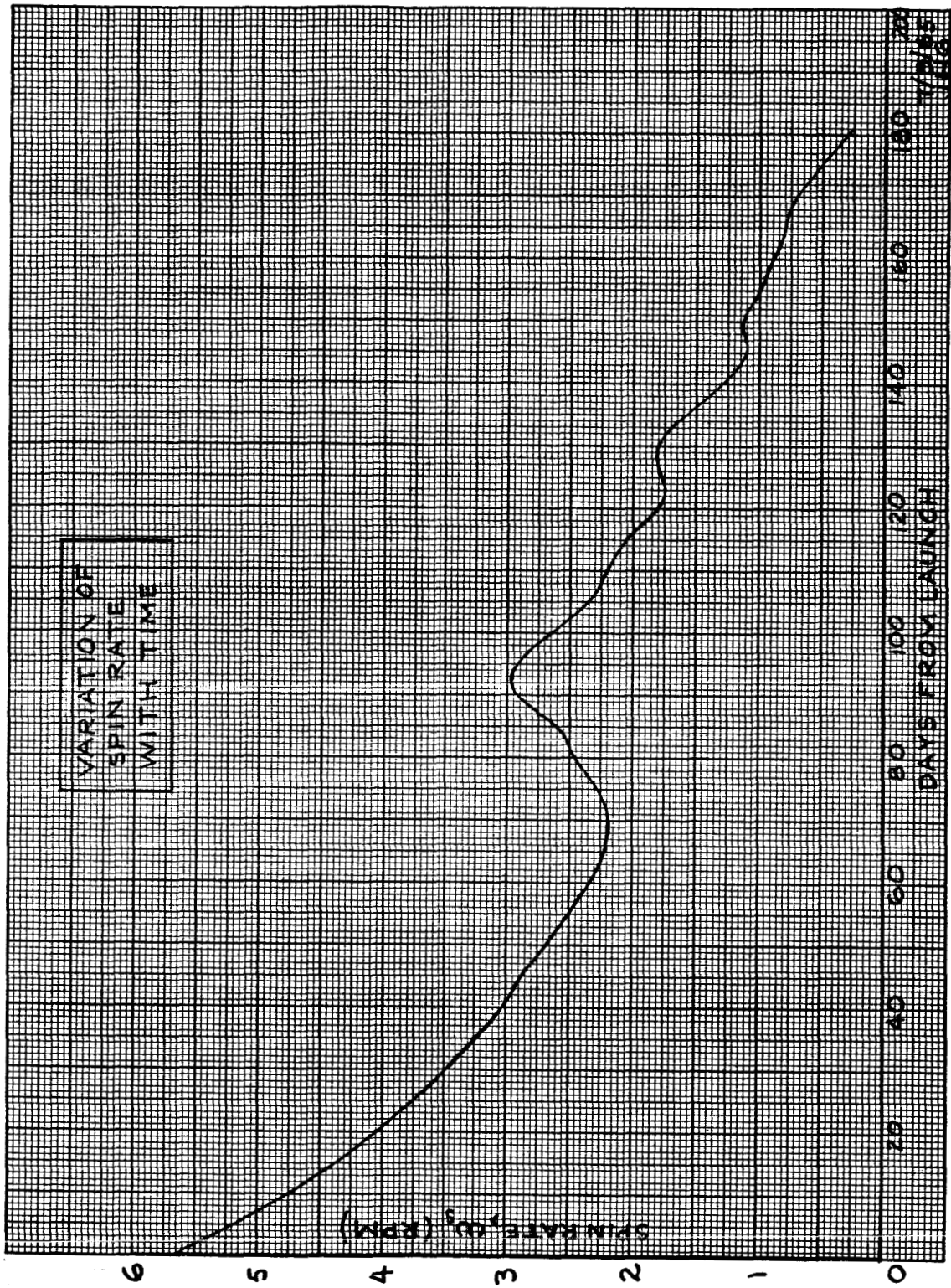


Figure 1 Variation of Spin Rate With Time

- a. aerodynamic
- b. solar radiation
- c. magnetic

Mr. David Blanchard of GSFC has made an analysis (unpublished at the date of this writing) of Ariel II spin rate performance. He established that magnetic torques were not significant and could be disregarded. He concluded that aerodynamic torques were the only significant factors in altering the spin rate of the satellite. Mr. Blanchard finally developed an equation which described the spin rate performance of Ariel II solely on the basis of the aerodynamic torques provided by the solar paddles and the galactic noise antenna. His developed spin rate curve closely matched the actual spin rate curve of Ariel II for the 200-day period considered. His spin rate analysis and equation were, however, based entirely on the assumption that the spin axis orientation of the satellite remained fixed in space for the entire 200-day period.

It becomes evident, however, upon reference to Figure 2, that the actual solar aspect angle differs markedly from the anticipated angle. This variation can only be explained by distinct variations in spin axis orientation. Although the vehicle is spin-stabilized, the spacecraft orientation varies from its initial direction as will be developed later. This variation, although minimized by the satellite spin, is a significant influence on spin deceleration.

An important aspect of the spin rate characteristic is that there are three definite periods of satellite spin-up. Positive spin accelerations can only be achieved by adding energy to the system. Aerodynamic and solar radiation forces are both capable of increasing the angular momentum of the satellite, whereas passive magnetic forces are incapable of such action.

The ensuing sections will estimate the aerodynamic and solar radiation effects on the satellite in relation to the spin rate performance. It will be shown that these effects can explain the spin-down and spin-up characteristics of Ariel II.

### 2.3.1 Equivalent Air Density

Inasmuch as aerodynamic forces were suggested by previous investigations as being the largest contributors to spin accelerations, air density, an important subsidiary parameter, needed definition. The air density

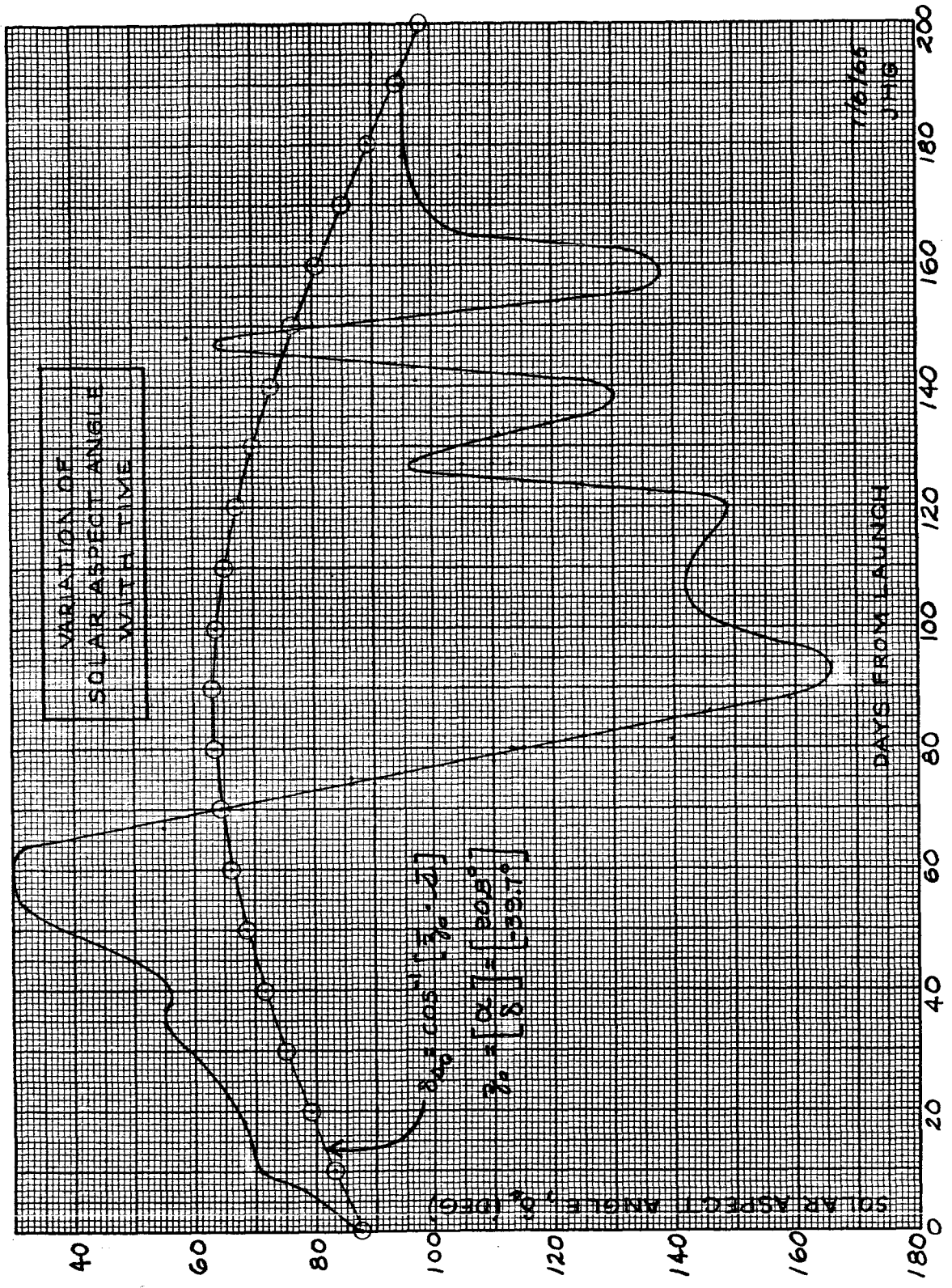


Figure 2 Variation of Solar Aspect Angle With Time

encountered by Ariel II is continuously variable since the orbit is eccentric ( $e > 0.07$ ).

Ref. 1<sup>1</sup> provides estimated air density data which considers variations due to:

- a. altitude - - in increments of 20 km
- b. time of day - - in two-hour increments
- c. solar activity - - in ten graduated levels.

In order to calculate aerodynamic forces it is desired to establish an equivalent mean value of air density which can be considered to be operating over the full orbit, although it is understood that most of the aerodynamic momentum change actually occurs near perigee.

It is estimated that the average solar flux in the 10.7 cm region over the dates of interest (3/27/64 to 10/13/64) is  $75 \times 10^{-22} \frac{\text{W/m}^2}{\text{cps}}$ . This value of solar activity is equivalent to Model 2<sup>1</sup>, corresponding to a level of very low solar activity.

The density was averaged over a 24-hour period for each increment of altitude from 290 to 500 km using the densities of Model 2, thereby providing a mean daily value of density for each altitude. A curve was then plotted of log density vs altitude to provide a smooth function of the density characteristic.

The eccentric anomaly, E, was then calculated for each altitude using the relation:

$$\frac{r}{a} = 1 - e \cos E$$

or:

$$E = \cos^{-1} \left[ \frac{1}{e} (1 - r/a) \right] \quad (1)$$

The mean anomaly, M, is obtained for each altitude for the case where  $M_0 = 0$  by using the relation:

$$M = E - e \sin E \quad (2)$$

1. Harris, I. and Priester, W., The Upper Atmosphere in the Range from 120 to 800 km. Inst. for Space Studies, GSFC, NASA. August 1964.

The orbital time corresponding to each altitude is then calculated for the case where  $t_0 = 0$  from the formula:

$$M = \mu t \quad (3)$$

and the mean orbital motion is:

$$\mu = \frac{2\pi}{T_a} \quad (4)$$

where:

$$T_a = \text{anomalistic period.}$$

A curve of altitude vs time was plotted to provide a smooth function of this relation. Using altitude as the common factor, a curve of density as a function of time was drawn. The area under this curve provides the time integral of density per orbit:

$$I\rho = \int_0^T \rho dt = 1.55 \times 10^{-10} \frac{\text{kg/m}^3 \times \text{min}}{\text{orbit}} \quad (5)$$

The equivalent mean density,  $\rho_{eq}$ , which is the density averaged over a full orbit, but which is considered to act only at perigee, is determined:

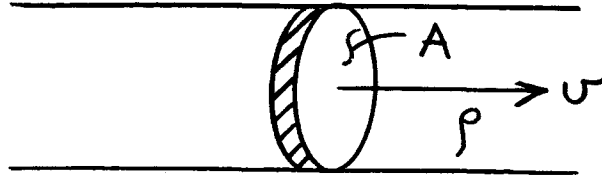
$$\begin{aligned} \rho_{eq} &= I\rho / T_a \\ &= 1.53 \times 10^{-12} \frac{\text{kg}}{\text{m}^3} \end{aligned} \quad (6)$$

This density value may be multiplied by actual orbit time to obtain accumulative effects. Use of perigee position and velocity conditions will not introduce significant errors, since the principal aerodynamic forces occur near perigee.

### 2.3.2 Aerodynamic Forces

The aerodynamic forces developed by complete gas molecule absorption by the paddle are derived first in this section. From this point, equations are generated for the three possible cases of: complete specular reflection of the gas molecules by the paddles; diffuse reflection of the gas molecules; and a combination of these two.

Assume a flat plate of frontal area,  $A$ , moving at velocity,  $v$ , through a stationary medium of free gas molecules of mass density,  $\rho$ .



According to the continuity equation the steady-state air mass flow past the plate is:

$$\dot{m} = \rho A v \quad (1)$$

If the impinging gas molecules were completely absorbed, the reaction force that would develop on the plate as a consequence of the rate of change of momentum is:

$$\begin{aligned} F &= \frac{d}{dt} (m v) \\ &= \dot{m} v \end{aligned} \quad (2)$$

Substituting (1) into (2) and considering that  $v$  is actually in the direction of vehicle motion, the reaction force vector is:

$$\bar{F} = - \rho A v^2 \bar{v} \quad (3)$$

where:

$$\bar{v} = \text{unit vector of plate velocity}$$

This reaction force is the aerodynamic drag force that would develop for perfect gas absorption. An equivalent drag coefficient,  $C_D$ , of 2 could be used in the familiar drag force equation,  $F = C_D A \frac{\rho v^2}{2}$ . For a flat plate of surface area,  $S$ , (one side) inclined at angle,  $i$ , to the velocity vector:

$$A = S \cos i = S (\bar{v} \cdot \bar{n}) \quad (4)$$

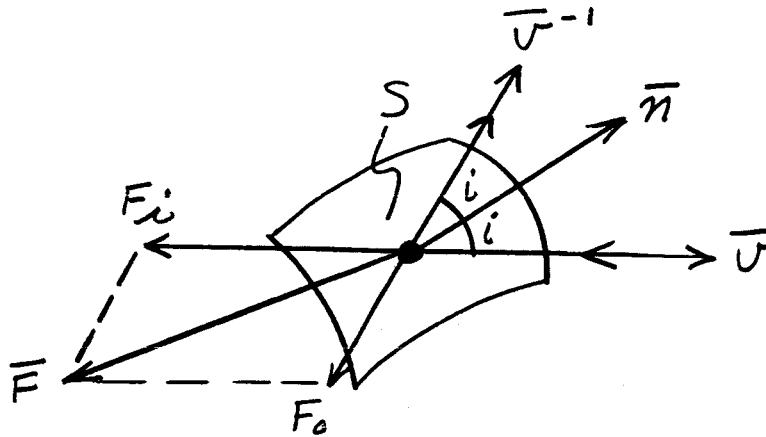
The aerodynamic drag force is then:

$$\bar{F} = - S (\bar{v} \cdot \bar{n}) (\rho v^2) \bar{v}$$

where:

$$\bar{n} = \text{unit vector normal to surface.}$$

A. Specular Reflection



Assume specular reflection of reflectivity,  $r_s$ , of the gas molecules from the surface of area,  $S$ . This condition assumes that the gas molecule rebounds from the surface with no loss in momentum.

The reaction force due to the incident energy is:

$$\bar{F}_i = - S (\bar{v} \cdot \bar{n}) (\rho v^2) \bar{v} \quad (5)$$

This force is equal to that developed by complete absorption.

The force due to the reflected energy is:

$$\bar{F}_o = - r_s S (\bar{v} \cdot \bar{n}) (\rho v^2) \bar{v}^{-1} \quad (6)$$

The resultant force is:

$$\begin{aligned} \bar{F} &= \bar{F}_i + \bar{F}_o \\ &= -S (\bar{v} \cdot \bar{n}) (\rho v^2) (\bar{v} + r_s \bar{v}^{-1}) \end{aligned} \quad (7)$$

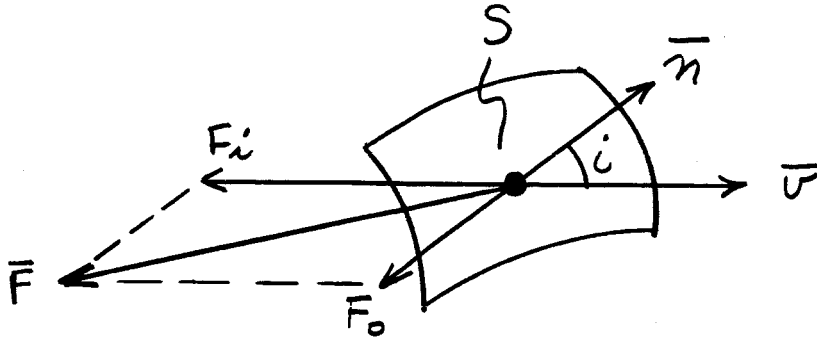
The normal force is:

$$\bar{F}_n = -S (\bar{v} \cdot \bar{n})^2 (\rho v^2) (1 + r_s) \bar{n} \quad (8)$$

For the special case where  $r_s = 1$ :

$$\bar{F}_n = -2 S (\bar{v} \cdot \bar{n})^2 (\rho v^2) \quad (9)$$

## B. Diffuse Reflection



Assume diffuse reflection of reflectivity,  $r_d$ , of the gas molecules from surface of area,  $S$ . This condition assumes that the gas molecules are initially absorbed then subsequently emitted from the surface at thermal velocity following Lambert's cosine law.

The reaction force due to the incident energy is:

$$\bar{F}_i = -S (\bar{v} \cdot \bar{n}) (\rho v^2) \bar{v} \quad (10)$$

The force due to the reflected energy is:

$$\bar{F}_o = -\frac{2}{3} r_d S (\bar{v} \cdot \bar{n}) (\rho v^2) \bar{n} \quad (11)$$

The resultant force is:

$$\bar{F} = -S (\bar{v} \cdot \bar{n}) (\rho v^2) \left( \bar{v} + \frac{2}{3} r_d \bar{n} \right) \quad (12)$$

The normal force is:

$$\bar{F}_n = -S (\bar{v} \cdot \bar{n}) (\rho v^2) \left[ (\bar{v} \cdot \bar{n}) + \frac{2}{3} r_d \right] \bar{n} \quad (13)$$

## C. General Reflection

For the more general case let us assume that reflection of the gas molecules is partly specular and partially diffuse with reflectivities,  $r_s$ , and  $r_d$ , respectively. The resultant reaction force is:

$$\bar{F} = -S (\bar{v} \cdot \bar{n}) (\rho v^2) \left[ \bar{v} + r_s \bar{v}^{-1} + \frac{2}{3} r_d \bar{n} \right] \quad (14)$$

The normal force is then:

$$\begin{aligned}\bar{F}_n &= -S (\bar{v} \cdot \bar{n}) (\rho v^2) \left[ (\bar{v} \cdot \bar{n}) + r_s (\bar{v} \cdot \bar{n}) + \frac{2}{3} r_d \right] \bar{n} \\ \bar{F}_n &= -S (\bar{v} \cdot \bar{n}) (\rho v^2) \left[ (1 + r_s) (\bar{v} \cdot \bar{n}) + \frac{2}{3} r_d \right] \bar{n} \quad (15)\end{aligned}$$

For the practical case of the satellite in orbit, it appears that there will be no significant molecular absorption since this would result in a continual accumulation of gas molecules. It is likely that the reflection process consists in part of specular reflection and the remainder of diffuse reflection. Since the emitting surface is at relatively low temperature the exit molecular velocity is statistically much lower than the entrance velocity. Thus the diffuse reflection effects can be effectively disregarded. The normal force can finally be obtained from equation (8) while allowing for operation from either side of the surface.

$$\bar{F}_n = -S (\bar{v} \cdot \bar{n}) \left| \bar{v} \cdot \bar{n} \right| (\rho v^2) (1 + r_s) \bar{n} \quad (16)$$

The equivalent air density was previously determined to be:

$$\rho_{eq} = 1.53 \times 10^{-12} \text{ kg/m}^3$$

Because of the eccentricity of the orbit the aerodynamic forces occur only near perigee. Therefore, the velocity at perigee can be used without appreciable error.

$$v_p = 8.01 \text{ km/sec}$$

The value of the aerodynamic terms can then be obtained:

$$(\rho_{eq} v^2) = 9.78 \times 10^{-5} \text{ nt/m}^2$$

and:

$$S (\rho_{eq} v^2) = 1.52 \times 10^{-5} \text{ nt} \quad (\text{for each paddle})$$

### 2.3.3 Aerodynamic Spin Torque and Acceleration

#### I. Solar Paddles

The limiting value of aerodynamic normal force on the solar paddles is obtained by assuming that:

- a. the satellite spin axis,  $\bar{z}$ , is aligned to the perigee velocity vector,  $\bar{v}_p$

b. the specular reflection coefficient,  $r_s$ , is 100 percent

The aerodynamic normal force on each paddle is:

$$F_n = -2S (\rho_{eq} v^2) \cos i \quad | \quad \cos i \quad | \quad (1)$$

1. Paddle #1 (or #3) where  $i = 67.4^\circ$ :

$$F_{n1} = -4.30 \times 10^{-6} \text{ nt}$$

2. Paddle #2 (or #4) where  $i = 59.8^\circ$ :

$$F_{n2} = -7.69 \times 10^{-6} \text{ nt}$$

The consequent aerodynamic torque about the satellite axis produced by the four solar paddles is:

$$\begin{aligned} T_z &= 1.122 F_{n1} + 1.164 F_{n2} & (2) \\ &= -1.38 \times 10^{-5} \text{ nt-m} \end{aligned}$$

This value of spin torque is averaged over the entire orbit.

The satellite is spin-accelerated by these aerodynamic forces acting on the solar paddles. The equivalent aerodynamic acceleration about the spin axis averaged over the orbit is:

$$\begin{aligned} \alpha_z &= \dot{\omega}_z \\ &= T_z / I_z \\ &= -2.13 \text{ rad/sec}^2 \\ &= -0.176 \text{ rpm/day} \end{aligned} \quad (3)$$

The maximum spin-down rate of the actual satellite--occurring directly after orbital injection where the angle,  $\phi$ , between  $\bar{z}$  and  $\bar{\sigma}_p$  is 7 deg -- is:

$$\dot{\omega}_s (\text{max}) = -0.10 \text{ rpm/day}$$

It is thus seen that aerodynamic torques are capable of producing the spin-down rates actually experienced by the satellite.

If we assume that the maximum aerodynamic torque produced by the solar paddles is attenuated by a  $\cos \phi \quad | \quad \cos \phi \quad |$  relation then we can account for the initial misalignment between  $\bar{z}$  and  $\bar{\sigma}_p$  and can estimate the specular reflectivity based on the assumption that the spin-down is due solely to these paddle forces:

$$\frac{1 + r_s}{2} = \frac{0.10}{0.176 \cos^2 7^\circ}$$

which provides an estimated specular reflectivity of:

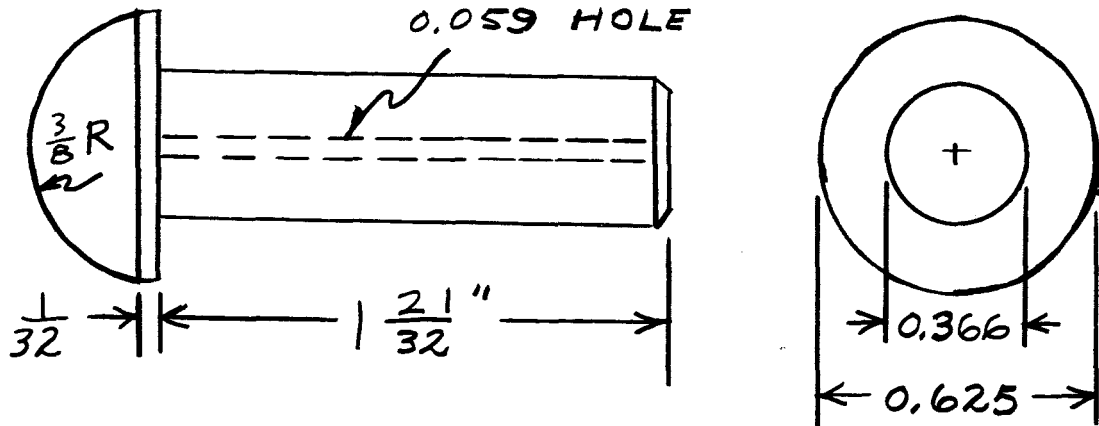
$$r_s = 0.15$$

It should be emphasized that the solar paddles are equally as capable of causing the satellite to spin up as indeed the satellite actually does. For example, on the 85th day the spin acceleration is +0.05 rpm/day — half the maximum spin-down value.

## II. Galactic Noise Antenna

The galactic noise dipole antenna consists of two weights each of which is attached to a stranded wire. The centrifugal acceleration of the weights maintains the antenna extended at a diameter of 130 ft.

Each weight has the following dimensions:

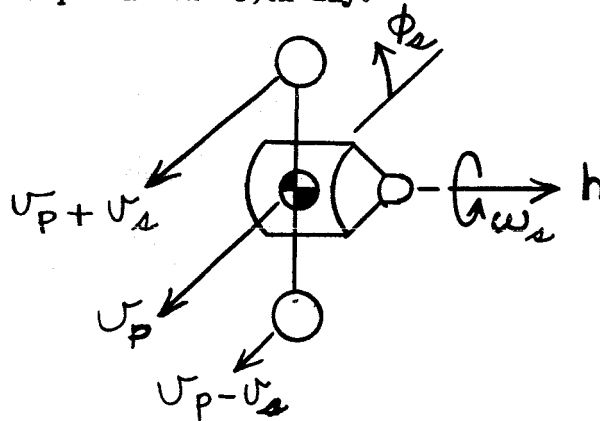


The projected (broadside) area of each weight is:

$$A = 0.723 \text{ in}^2$$

The wire has an outside diameter of 0.057 in. For aerodynamic drag estimates consider the antenna wire to be attached at the spin axis.

The maximum despin torque condition occurs when the spin axis,  $\bar{z}$ , is normal to the perigee velocity vector,  $\bar{v}_p$ , i.e., when  $\phi = 90$  deg. This condition is considered to occur at points of zero slope on the spin rate curve of Figure 1, for example at the 69th day.



The component of velocity normal to either weight is

$$v_n = \omega_s l + v_p \sin \phi_s \quad (1)$$

The normal force of the two weights assuming for convenience that  $r_s = 0$  is:

$$\begin{aligned} F &= -A (\rho_{eq} v^2) \\ &= -A \rho \left[ (\omega_s l + v_p |\sin \phi_s|)^2 \right. \\ &\quad \left. - (\omega_s l - v_p |\sin \phi_s|)^2 \right] \\ &= -4A \rho v_p \omega_s l \sin \phi_s \end{aligned} \quad (2)$$

The average value of this normal force is

$$F_{av} = -\frac{8}{\pi} A \rho v_p \omega_s l \quad (3)$$

The corresponding aerodynamic torque about the spin axis due to the two weights is:

$$T = -\frac{8}{\pi} A \rho v_p \omega_s l^2 \quad (4)$$

Now consider the elemental normal force of the two wires:

$$dF = -\frac{8}{\pi} a \rho v_p \omega_s r dr \quad (5)$$

where:  $a$  = projected area/ft of wire

The corresponding elemental torque experienced by the two wires is:

$$dT = -\frac{8}{\pi} a \rho v_p \omega_s r^2 dr \quad (6)$$

Integrating over the length of the wires the aerodynamic torque is:

$$\begin{aligned} T &= -\frac{8}{\pi} a \rho v_p \omega_s \int_0^l r^2 dr \\ &= -\frac{8}{3\pi} A_{\text{wire}} \rho v_p \omega_s l^2 \end{aligned} \quad (7)$$

The combined aerodynamic torque of the weights and wires is then:

$$T = -\frac{8}{\pi} \rho v_p \omega_s l^2 (A_{\text{wt}} + \frac{1}{3} A_{\text{wire}}) \quad (8)$$

$$A_{\text{wt}} + \frac{1}{3} A_{\text{wire}} = 1.003 \times 10^{-2} \text{ m}^2$$

$$l = 19.81 \text{ m}$$

$$\rho = 1.53 \times 10^{-12} \text{ kg/m}^3$$

$$v_p = 8.01 \text{ km/sec}$$

$$\phi = 90 \text{ deg at } D = 69$$

$$\omega_{69} = 0.230 \text{ rad/sec (or 2.2 rpm)}$$

The aerodynamic torque produced by the weights and wires on the 69th day where the spin axis,  $\bar{z}$ , is normal to the perigee velocity vector,  $\bar{v}_p$ , is then calculated using equation (8):

$$T_{69} = -2.82 \times 10^{-8} \text{ nt-m}$$

The corresponding acceleration about the spin axis is:

$$\begin{aligned} \alpha_z &= T/I_z \\ &= -4.38 \times 10^{-10} \text{ rad/sec}^2 \\ &= -3.62 \times 10^{-4} \text{ rpm/day} \end{aligned}$$

This value corresponds to the condition of maximum magnitude of acceleration, but is still orders of magnitude lower than the maximum magnitude of acceleration produced by the solar paddles alone. A choice of  $r_s = 1.0$  would have only increased this magnitude by at most a factor of 2.

Additional aerodynamic torques are produced by other vehicle appendages but since their moment arms are small, so are their effects.

For all practical purposes the aerodynamic spin accelerations can be considered to be produced solely by the solar paddles.

As the direction of spacecraft orientation is reversed ( $\phi > 90$  deg), the relative wind on the solar paddles will develop a positive spin acceleration or spin-up condition of equivalent magnitude. The solar paddles, which act as a four-bladed propeller, provide the only means by which the spacecraft can increase its angular momentum. The center body and all the other spacecraft appendages are incapable of producing a positive spin acceleration.

#### 2.3.4 Solar Pressure Spin Torque and Acceleration

The solar pressure on a perfect absorber for normal incidence at earth orbit is:

$$\frac{S}{c} = 4.54 \times 10^{-6} \text{ nt/m}^2 \text{ (for absorptivity, } \alpha_j = 1)$$

Assume 100 percent specular reflection ( $r_s = 1$ ) and assume that  $\bar{z}$  is aligned to  $\bar{s}$  -- conditions which produce a maximum torque about the spin axis.

The normal force exerted by solar radiation on the solar paddles is provided by the relation:

$$F_n = -2 \left(\frac{S}{c}\right) S \cos i \left| \cos i \right| \quad (1)$$

For paddle #1 (or #3) where  $i = 67.4^\circ$ :

$$F_{n1} = -2.10 \times 10^{-7} \text{ nt}$$

For paddle #2 (or #4) where  $i = 59.8^\circ$ :

$$F_{n2} = -3.60 \times 10^{-7} \text{ nt}$$

The consequent radiation spin torque developed by the four solar paddles for the case where  $\bar{z} = \bar{s}$  and  $r_s = 1$  is as previously determined:

$$\begin{aligned} T_z &= 1.122 F_{n1} + 1.162 F_{n2} \\ &= -6.54 \times 10^{-7} \text{ nt-m} \end{aligned} \quad (2)$$

The resulting maximum spin acceleration due to solar pressure on the solar paddles is:

$$\begin{aligned}\alpha_s &= \dot{\omega}_s = T_z/I_z \\ &= -1.01 \times 10^{-8} \text{ rad/sec}^2 \\ &= -8.34 \times 10^{-3} \text{ rpm/day}\end{aligned}$$

This value of spin acceleration is the maximum that could be achieved, since it is based on these assumptions:

- a. There is 100% reflection of the incident solar power;
- b. the reflection is purely specular; and
- c. there is 100% sunlight during the entire orbit.

In the actual case, the spin acceleration due to solar pressure will be less than this limiting value for the following reasons:

- a. the reflectivity of the solar panels is obviously less than 100% since a portion of the incident sunlight is converted to electrical power
- b. the solar aspect angle is never zero but instead has a minimum value of 30 deg at the 60th day
- c. the amount of sunlight during an orbit varies between 63 and 100 percent but is less than 70 percent for 68 percent of the time over the first 200 days.

Based on the above considerations, we can estimate the value of the spin acceleration on the 60th day to be:

$$\begin{aligned}\alpha_{60} &= -8.43 \times 10^{-3} \times 0.5 \cos^2 30^\circ \times 0.68 \\ &= -2.20 \times 10^{-3} \text{ rpm/day}\end{aligned}$$

This value of spin acceleration is only 2.2 percent of the maximum measured spin acceleration of -0.10 rpm/day. Maximum despin of Ariel II occurs on the first day, but at this time the solar aspect angle is 87 deg so that the solar effects are negligible at this time.

Thus we see that solar pressure effects are not a significant factor in causing satellite spin-down.

#### 2.4 Spacecraft Orientation

It is readily apparent, after reviewing the solar aspect angle as plotted in Figure 2, that the spacecraft orientation is definitely not fixed in

space. Although the satellite is a spin-stabilized vehicle -- spinning about its stable axis with a considerable angular momentum -- the craft is subject to definite disturbances which result in precession.

The purpose of this section of the report is to determine the most probable trajectory of spin axis orientation.

No attitude sensors were installed on Ariel II so attitude information must be inferred from known orbital elements, satellite spin rate (Figure 1) and solar aspect angle (Figure 2). These latter two characteristics were themselves deduced indirectly from telemetered data covering the first 200 days in orbit.

#### 2.4.1 Velocity Aspect Angle

It was previously determined in Section 5 of this report that the aerodynamic torques exerted by the solar paddles in the vicinity of perigee were responsible for essentially the entire spin rate behavior of the spacecraft. As a necessary step in establishing vehicle orientation it is desired to determine the velocity aspect angle (or angle of attack) as a function of time. This angle,  $\theta_v$ , is defined as that angle between the spacecraft spin axis,  $\bar{z}$ , and the perigee velocity vector,  $\bar{v}_p$ .

The acceleration characteristic about the vehicle spin axis, as illustrated by Figure 3, was obtained by differentiating the spin rate characteristic of Figure 1. As may be observed, the initial spin acceleration is -0.10 rpm/day--corresponding to a condition of maximum spin-down. The maximum spin-up occurs at the 85th day where the maximum spin-up is 0.05 rpm/day--half the magnitude of the original spin deceleration. Two other periods of positive spin acceleration occur.

Knowing the spin acceleration,  $\alpha_z$ , the aerodynamic torque that produced that acceleration may be readily calculated from the relation:

$$T_z = I_z \alpha_z \quad (1)$$

The problem then becomes one of determining the function relating vehicle angle of attack to the aerodynamic torque developed about the spin axis.

The two pairs of solar paddles are attached to the spacecraft struts with different angular settings. Geometrical interference or shadowing becomes

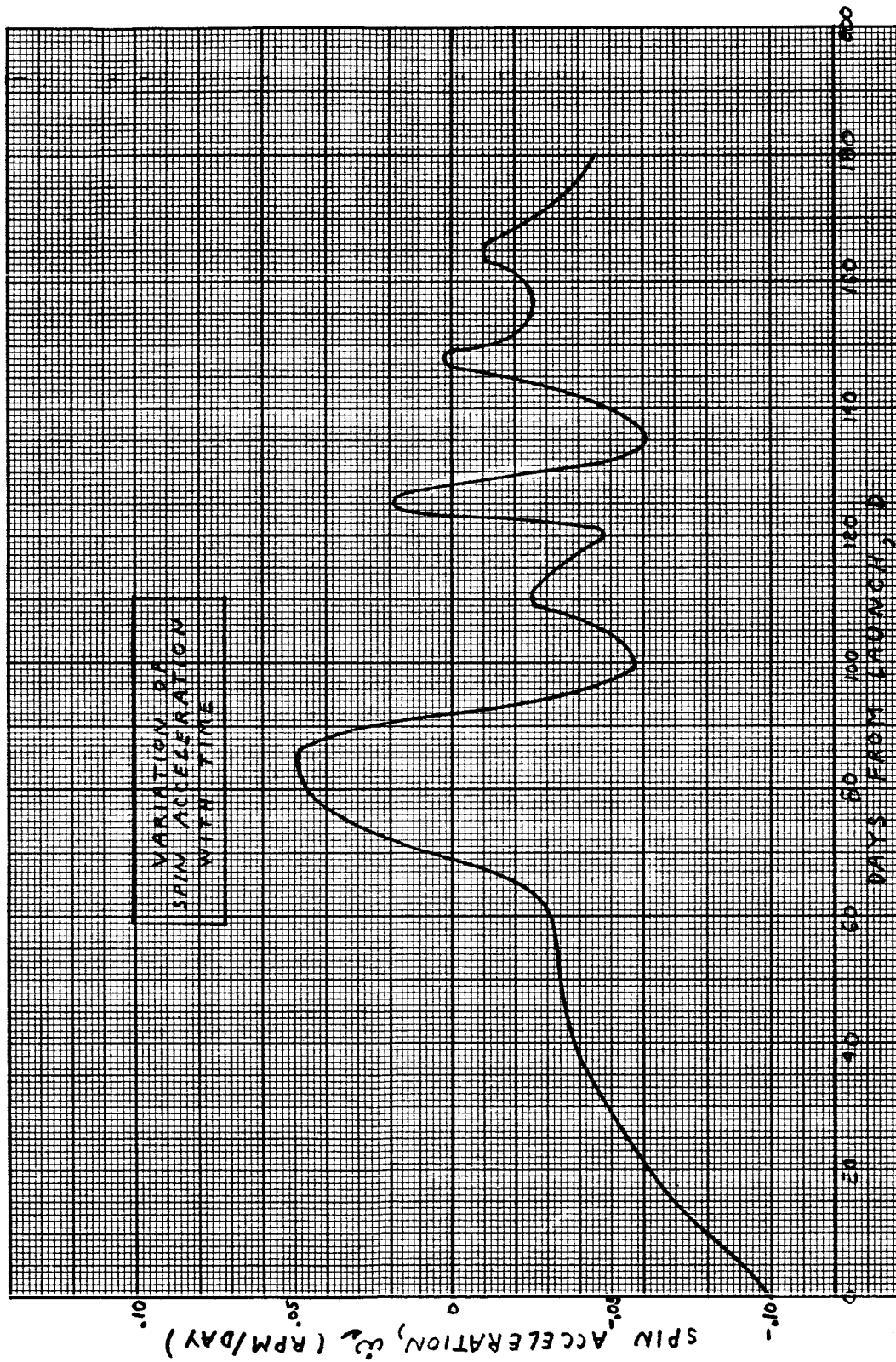
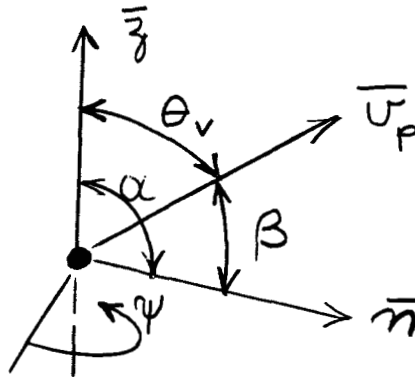


Figure 3 Variation of Spin Acceleration With Time

a definite factor in modifying paddle torques. Depending on the vehicle aspect angle the center body may cyclically shadow variable portions of the paddles during part of the spin revolution while the solar paddles also shadow each other in a cyclic and complex fashion. Because of the complexity of the shadow problem, and in view of the relative lack of precision in derived pertinent data, a rigorous investigation could not be justified.

In deriving the aerodynamic force exerted on a spinning paddle consider the following diagram:



The instantaneous angle between the perigee velocity vector,  $\vec{v}_p$ , and the individual paddle normal,  $\vec{n}$ , may be calculated from the relation:

$$\cos \beta = \cos \theta_v \cos \alpha + \sin \theta_v \sin \alpha \cos \psi \quad (2)$$

where  $\psi$  is spin angle.

Since spin torques are determined only by forces normal to the paddles, the general normal force equation for an individual paddle is:

$$F_n = S \rho v^2 \left[ (1 + r_s) \cos \beta / \cos \beta + \frac{2}{3} r_d \cos \beta \right] \quad (3)$$

As indicated in Section 2.3.2 the effects of diffuse aerodynamic reflections are negligible, so equation (3) can be effectively simplified to read:

$$F_n \doteq S \rho v^2 \left[ (1 + r_s) \cos \beta / \cos \beta \right] \quad (4)$$

The above equation is valid only for the theoretical case of no shadowing. In the actual case equation (4) must be modified to take shadowing into account. Those portions of equations (3) and (4) within brackets were evaluated by integrating over one spin revolution for various values of  $\theta_v$  and for three completely arbitrary combinations of reflectivities ( $r_s = 1, r_d = 1,$

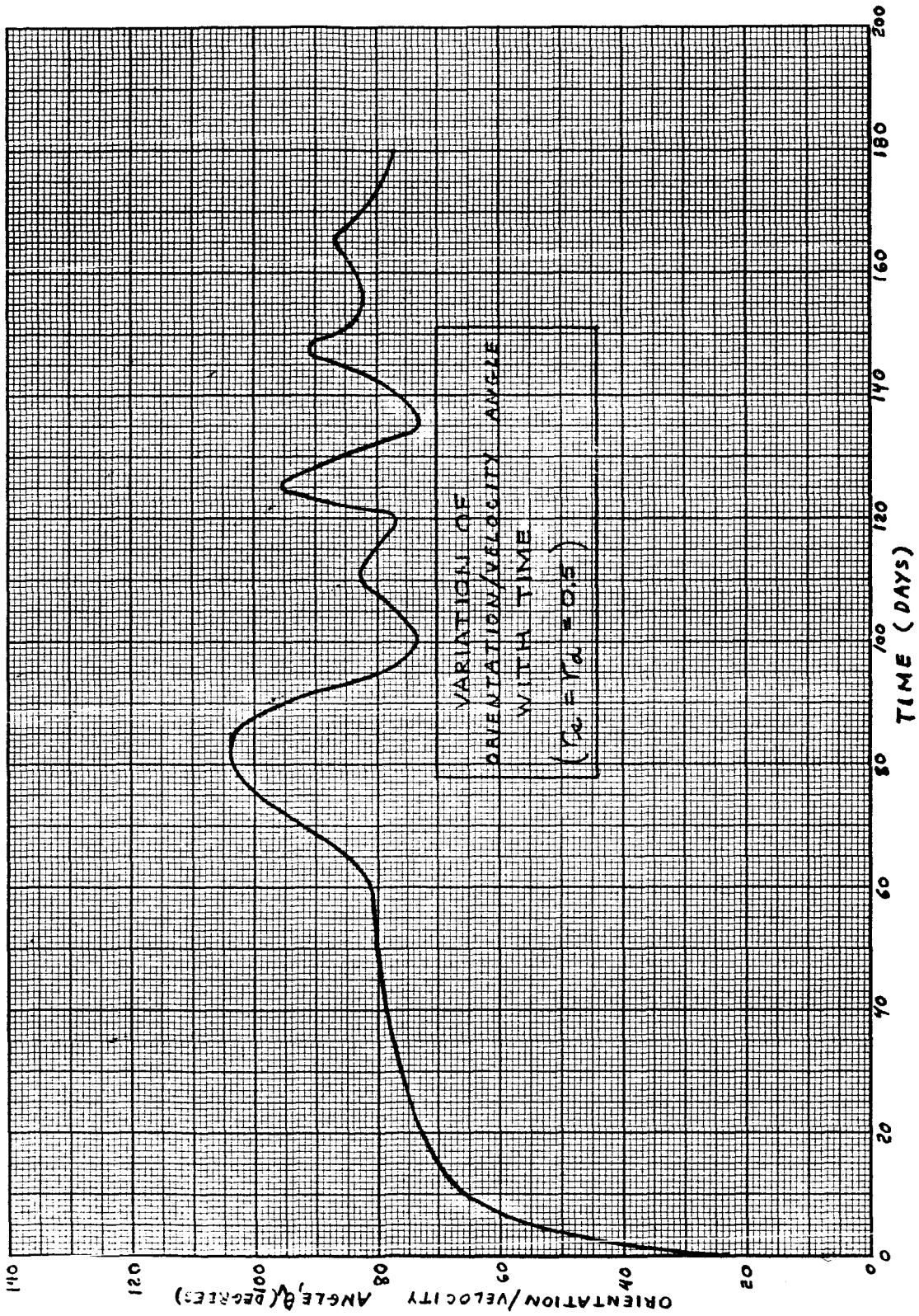


Figure 4 Variation of Orientation/Velocity Angle With Time

and  $r_s = r_d = 0.5$ )\* The spin torque developed by the four solar paddles can then be determined by applying the paddle normal forces to the torque equation previously developed in Section 2.2:

$$T = 1.122 F_{n1} + 1.164 F_{n2} \quad (\text{nt-m}) \quad (5)$$

This torque variation, which is a function of the velocity aspect angle,  $\theta_v$ , can be applied to the actual spin torque history of the satellite to obtain the velocity aspect angle,  $\theta_v$ , as a function of days from launch. An example is presented in Figure 4 for the arbitrary case where  $r_s = r_d = 0.5$ . Shadowing effects were not included in developing this curve.

A simpler and more intuitive approach was also made by assuming that the actual aerodynamic spin torque developed by the solar paddles varied simply as a function of velocity aspect angle,  $\theta_v$ , as indicated below:

$$T = S \rho v^2 (1 + r_s) \cos \theta_v \left| \cos \theta_v \right| \quad (6)$$

The results of equation (6) when combined with the spin torque history of Ariel II are presented in Figure 5 which presents the velocity aspect angle as a function of days from launch. Subsequently discussed analysis lends more credibility to the results of Figure 5 than to those of Figure 4.

#### 2.4.2 Spin Axis Orientation

The orientation of the spacecraft may finally be determined based on a knowledge of these four parameters:

- a. solar position
- b. solar aspect angle
- c. position of perigee velocity vector
- d. velocity aspect angle.

The position of the sunline,  $\bar{s}$ , for the 200-day period is plotted in celestial coordinates in the curve of Figure 10 of the Phase II report. The time plot of solar aspect angle,  $\delta_s$ , is shown by Figure 3 of the Phase II report. The direction of the perigee velocity vector,  $\bar{v}_p$ , is presented in celestial coordinates for the 200-day period by Figure 12 of Phase II report. The velocity

---

\*This analysis was carried out prior to concluding that  $r_d$  can be disregarded as stated in section 2.3.2. Taking  $r_{d0}$  will change the numerical results of the present section somewhat, but will not alter the conclusions of the report.

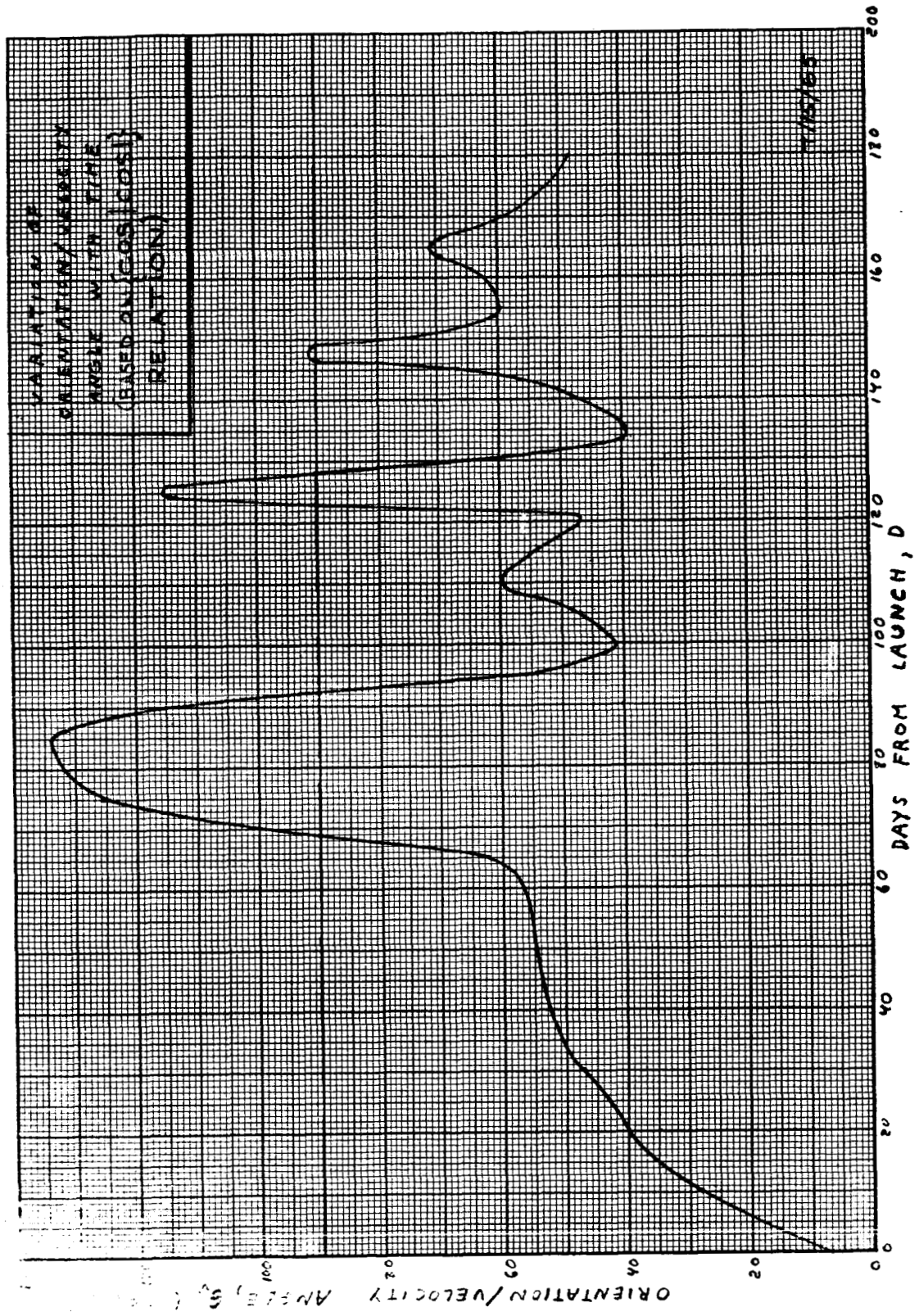
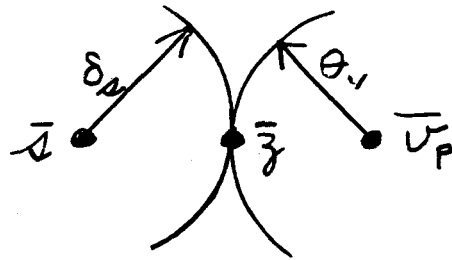


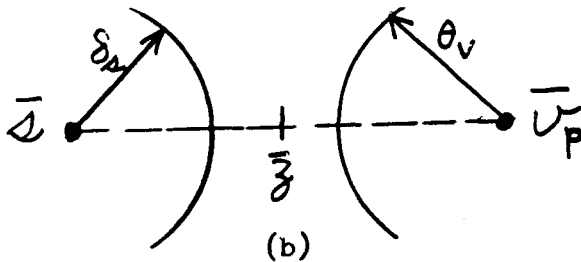
Figure 5 Variation of Orientation/Velocity Angle With Time  
 (Based on  $|\cos|$  Relation)



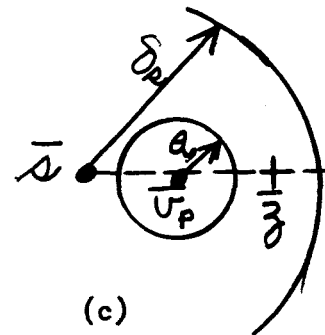


(a)

Occasionally, due to incompatible data, the situation presented by either figure (b) or (c) will develop, in which case the singular point,  $\bar{z}$ , is arbitrarily taken as shown:



(b)



(c)

The element of uncertainty of point selection is removed at each of these unique points. The initial orientation,  $\bar{z}_0$ , as described in Section 2.2.9 of the Phase II report, provides an accurate, well defined starting point. The procedure used to describe the most probable trajectory of the orientation vector was to plot all points in celestial coordinates -- declination vs right ascension -- with time indicated at each point. The more likely points were selected on the basis of a smooth, consistent progression of points. In most cases there is little doubt about which point is the more probable one. The most probable trajectory of spacecraft orientation,  $\bar{z}$ , is portrayed in celestial coordinates by Figure 6. Points are plotted approximately every five days. For reference purposes curves of sunline position,  $\bar{s}$ , and direction of perigee velocity vector,  $\bar{v}_p$ , are also displayed on this plot. Interestingly, the aerodynamic model--used to derive velocity aspect angle,  $\theta_v$ , --which provided the most compatible, consistent and smooth orientation data was that corresponding to figure 5 which was based on the  $\cos \theta_v \mid \cos \theta_v \mid$  relation and which is certainly only an approximation of the true picture.

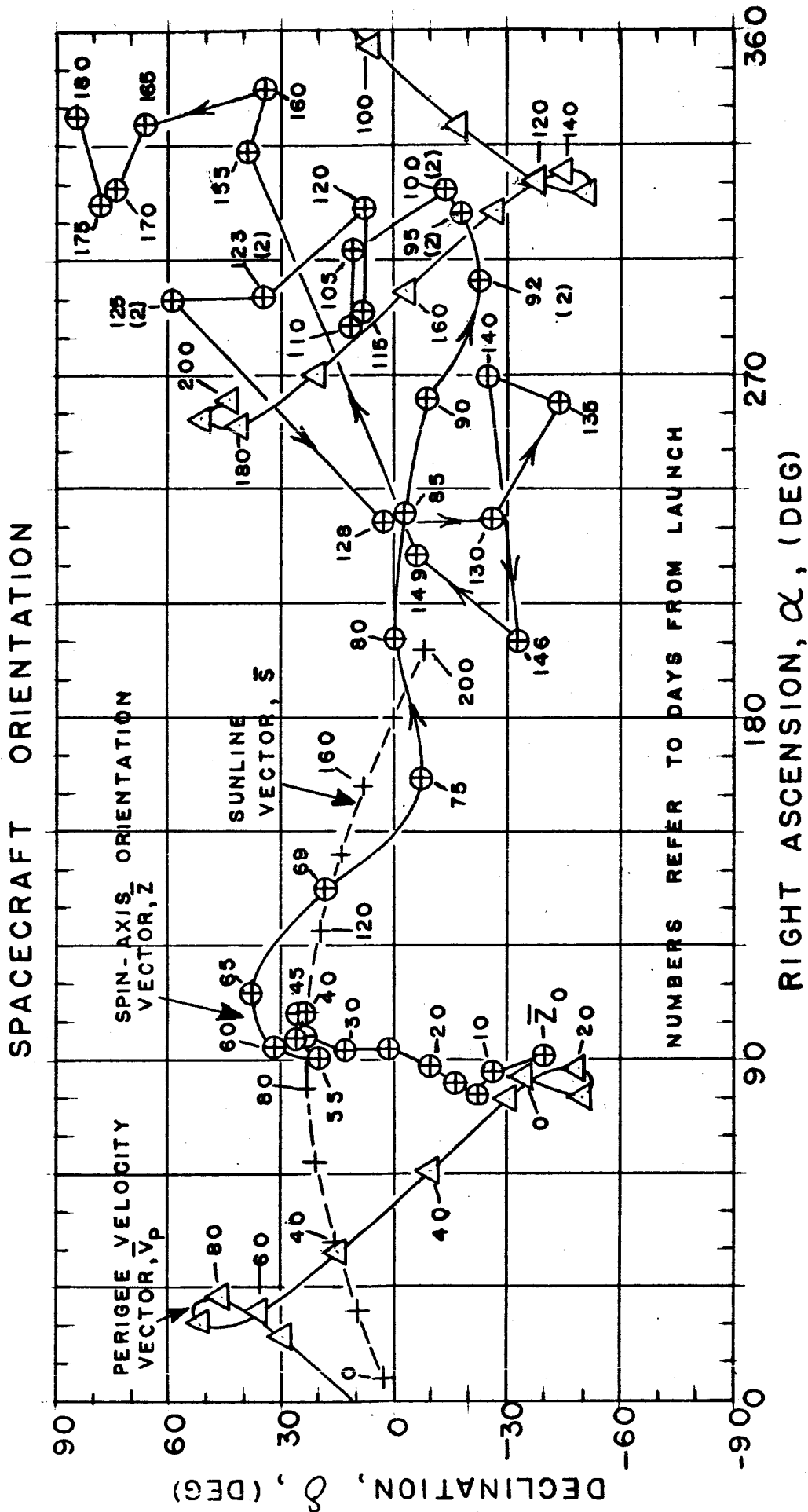


Figure 6 Spacecraft Orientation

The spin-axis orientation vector,  $\bar{z}$ , is seen to move slowly from the initial position,  $\bar{z}_0$ . As time progresses (and the spin rate decreased) the spin axis moves more rapidly in space and establishes a more erratic motion. The orientation vector appears to wander about in a random fashion, but the amount of actual orientation wander over the 180-day period considered is surprisingly small:

| <u>Celestial<br/>Coordinate</u> | <u>Total Angular<br/>Change (deg)</u> |
|---------------------------------|---------------------------------------|
| right ascension                 | 254                                   |
| declination                     | 124                                   |

Thus while the spacecraft orientation does not remain fixed in space, Ariel II does appear to be reasonably well space-stabilized over the half-year period under consideration.

## 2.5 Spacecraft Stability

Ariel II was initially spun up about its Z-axis, the axis of maximum moment of inertia. This spin axis is definitely the stable axis -- maintaining its stability despite energy dissipation within flexing spacecraft members and appendages. There is no definite evidence to indicate that the craft spun about any axis other than the principal Z-axis, although it must be admitted there were isolated bits of inconsistent telemetered data which would have been easier to explain if the craft had been tumbling about.

The spacecraft may be considered to consist of two separate spinning systems:

- a. a relatively rigid center body with fixed appendages
- b. the galactic noise dipole antenna composed of weights and thin flexible wires.

The antenna is spinning in a plane which is presumably normal to the spin or Z-axis of the spinning center body. The antenna weights due to centrifugal acceleration resulting from the spin rate ensure that the antenna retains the form of a flat dipole. The antenna wires are attached to the center body and are then fed through the two diametrically opposed galactic antenna booms which act as wire guides. The booms are in turn rigidly fastened to the center body.

The center body by itself is also a stable body and will thus tend to spin about its own Z-axis. If we now consider a disturbance torque to act upon the center body, we might expect a consequent angular precession to develop about the momentum vector of the center body and about the undisturbed antenna axis of rotation. Any precessional movement of the center body relative to the antenna spin axis would as a result of the constraint offered by the boom guides cause the antenna weights to be reeled in. This action would be strongly opposed by the centrifugal acceleration of the weights. It may be concluded therefore that the entire spacecraft is essentially a rigid body system, i.e., the spin axis of the center body maintains itself in virtual alignment with the spin axis of the entire satellite system. Any disturbance torques acting on the center body will be resisted by the total angular momentum of the spacecraft, and the entire spacecraft will accordingly precess as a single physical unit.

## 2.6 Precession Torques

It becomes apparent after reviewing Section 2.4.2 and Figure 6 in particular that the orientation of Ariel II did not remain fixed in space, as one might expect of a spin-stabilized craft, but instead wandered about in space in a seemingly random fashion. Nevertheless, the amount of wander over the 180-day period for which data was available proved to be surprisingly small, indicating the effectiveness of the spin stabilization. As mentioned in the previous section the maximum departure from the initial orientation vector,  $\bar{z}_0$ , was only 254 deg in right ascension and 124 deg in declination.

The maximum rate of change of spacecraft pointing direction is on the order of 27 deg/day between the 125th and the 128th day where the spin rate is 1.8 rpm.

Even though Ariel II did not in the first 180 days deviate a great deal from its initial direction in space, the fact remains that it did move about to some extent. This change in Ariel II orientation can be explained as the accumulated effect of the several precessional motions developed by the vehicle as a consequence of disturbance torques exerted on the spacecraft. The disturbance torques likely to be a factor in Ariel II's attitude behavior include:

- a. gravity gradient
- b. aerodynamic
- c. solar radiation

Since the latter disturbance torque is similar in effect to aerodynamic disturbance torques but is considerably smaller in degree it will not be considered further.

The angle,  $\gamma$ , between the orbit vector,  $\bar{w}_o$ , and the spacecraft orientation vector,  $\bar{z}$ , was calculated at 10-day intervals and is plotted as a function of time in the curve of Figure 7. Although the angle oscillates back and forth, it is noted that its departure from a nominal 90-deg level is only +33 deg and -51 deg. It is also interesting to note in the case of Figure 5 that the velocity aspect angle,  $\theta_v$ , generally oscillates about a nominal 90-deg level also. Despite these two observations, there unfortunately is no definite trend toward any specific angular correspondence between the perigee radius vector,  $\bar{r}_p$ , and the orientation vector,  $\bar{z}$ .

Gravity gradient torques and aerodynamic disturbance torques will be briefly discussed in the following sections.

### 2.6.1 Gravity Gradient Torques

The dominant terms of the equations expressing the gravity gradient torques on the satellite are:

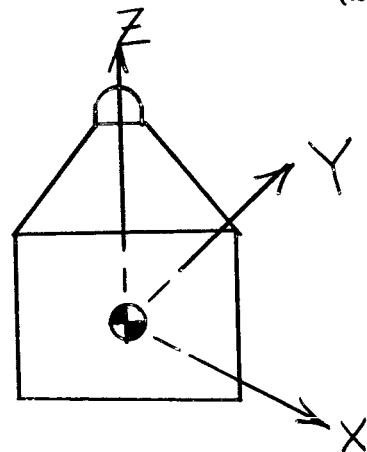
$$T_{G_x} = -\frac{3}{2} \frac{K}{r^3} (I_y - I_z) \sin 2 \theta_x \quad (1)$$

$$T_{G_y} = -\frac{3}{2} \frac{K}{r^3} (I_x - I_z) \sin 2 \theta_y \quad (2)$$

where:

$$K = 3.986 \times 10^5 \frac{\text{km}^3}{\text{sec}^2}$$

$$\begin{aligned} r_p &= R_e + h \\ &= 6371.3 + 289.5 \\ &= 6660.8 \text{ km} \\ a &= 7202 \text{ km} \end{aligned}$$



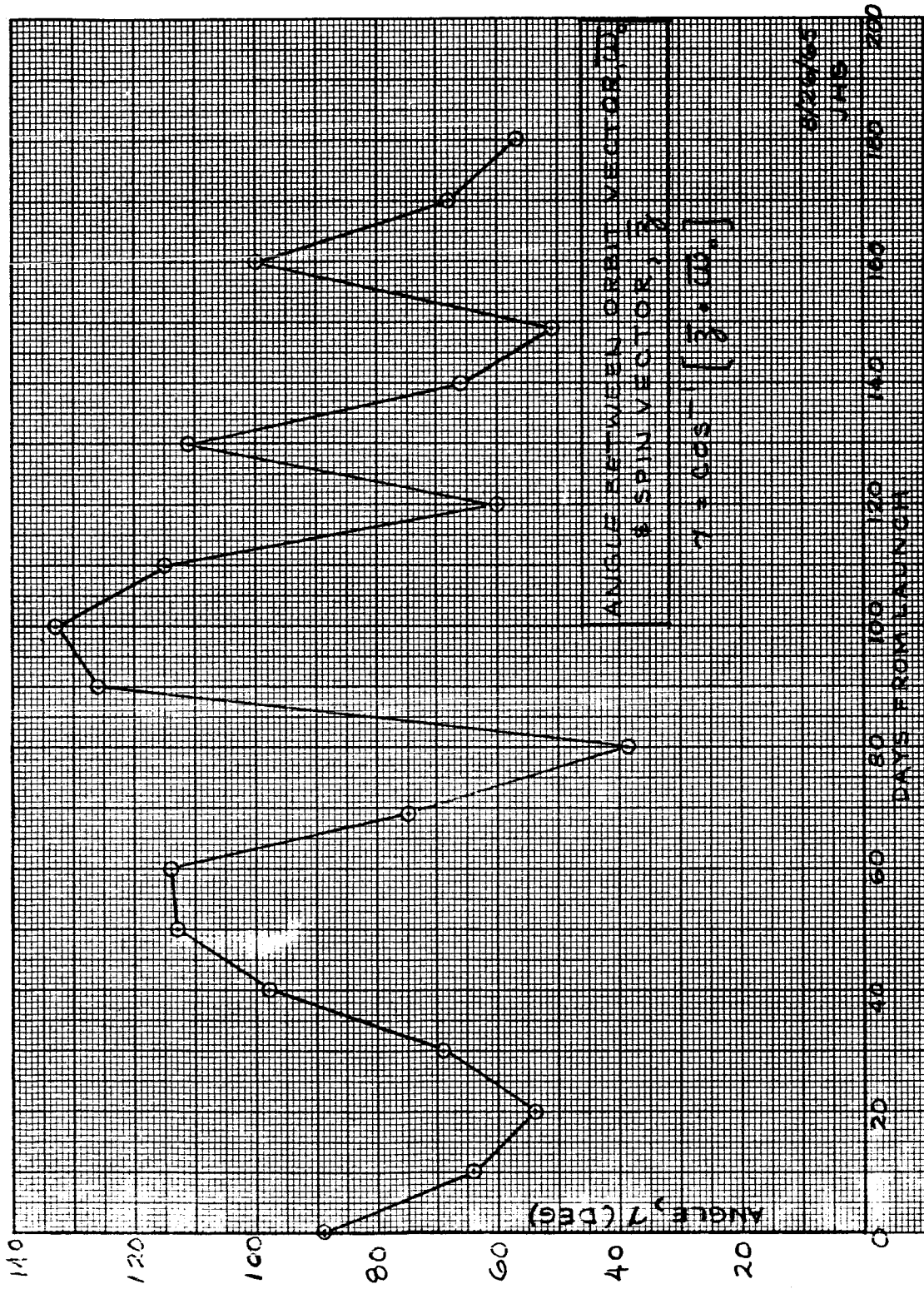


Figure 7 Angle Between Orbit Vector and Spin Vector

$$I_x = 61.79 \text{ Kg-m}^2$$

and

$$I_y = 8.68 \text{ Kg-m}^2$$

$$I_z = 64.70 \text{ Kg-m}^2$$

To obtain the mean gravity gradient torque during each orbit, substitute the semi-major axis,  $a$ , for  $r$ :

$$\frac{2}{3} \frac{K}{a^3} = \frac{2}{3} \times \frac{3.986 \times 10^5}{(7.202 \times 10^3)^3} \frac{\text{km}^3/\text{sec}^2}{\text{km}^3}$$

$$= 1.61 \times 10^{-6} \text{ sec}^{-2}$$

The torques introduced by gravity-gradient are then:

$$T_{G_x} = 1.61 \times 10^{-6} (64.70 - 8.68) \sin 2 \theta_x$$

$$= \underline{9.01 \times 10^{-5} \sin 2 \theta_x} \text{ nt-m} \quad (3)$$

$$T_{G_y} = 1.61 \times 10^{-6} (64.70 - 61.79) \sin 2 \theta_y$$

$$= \underline{4.68 \times 10^{-6} \sin 2 \theta_y} \text{ nt-m} \quad (4)$$

It is seen that  $T_{G_y}$  is much smaller than  $T_{G_x}$  and therefore  $T_{G_y}$  will be dropped from further consideration.

The gravity-gradient torque about the satellite's X-axis attempts to align the Z-axis to the local horizontal plane (normal to the local geocentric vertical). This torque acting on the spinning satellite produces a cyclic (related to spin angle) precession of the Z-axis about the local geocentric vertical. The Y-axis will attempt to align with the radius vector,  $\bar{r}$  (local vertical) since  $\bar{y}$  is the principal axis of least inertia.

### 2.6.2 Aerodynamic Precession Torque

The aerodynamic disturbance torque appears near the perigee condition each orbit. It is largely determined by the aerodynamic forces exerted on the four solar paddles and on the center body. Since the solar paddles have considerably longer moment arms, much of the aerodynamic torque is developed by the paddles, although the center body and solar paddles do shadow each other. The center-of-pressure of each paddle is alternately 0.559 m and 0.507 m below

the center-of-mass of the satellite--measured along the Z-axis. Since the solar paddles act like a trailing four-bladed propeller, the aerodynamic precession torque will strive to continually align the Z-axis with the perigee velocity vector. Because the satellite is spinning, an angular precessional rate will be developed normal to both the spin vector and the velocity vector. Using the arbitrary reflection characteristics of  $r_s = r_d = 0.5$  and assuming no shadowing, a rough estimate was made of the aerodynamic disturbance torque as a function of velocity aspect angle.

This approximate function is shown in Figure 8. As an example let us consider the case of the 128th day:

$$\begin{aligned}\theta_v &= 90 \text{ deg} \\ T &= 2.65 \times 10^{-5} \text{ nt-m (at } \theta_v = 90^\circ) \\ \omega_z &= 1.8 \text{ rpm (from curve of spin rate)} \\ &= 0.1882 \text{ rad/sec} \\ I_z &= 64.7 \text{ kg-m}^2\end{aligned}$$

The spin momentum is:

$$\begin{aligned}H_z &= I_z \omega_z \\ &= 64.7 \text{ kg-m}^2 \times 0.1882 \text{ rad/sec} \\ &= 12.19 \text{ nt-m-sec}\end{aligned}$$

Since the precession torque relation is:

$$T = \omega H_z$$

the rate of angular precession is:

$$\begin{aligned}\omega &= T/H_z \\ &= \frac{2.65 \times 10^{-5} \text{ nt - m}}{12.19 \text{ nt - m - sec}} \\ &= 2.18 \times 10^{-6} \text{ rad/sec} \\ &= \underline{10.8 \text{ deg/day}}\end{aligned}$$

The above estimate of angular precession rate of the spacecraft orientation vector illustrates that aerodynamic torques are capable of producing much of the attitude drift rate experienced by Ariel II.

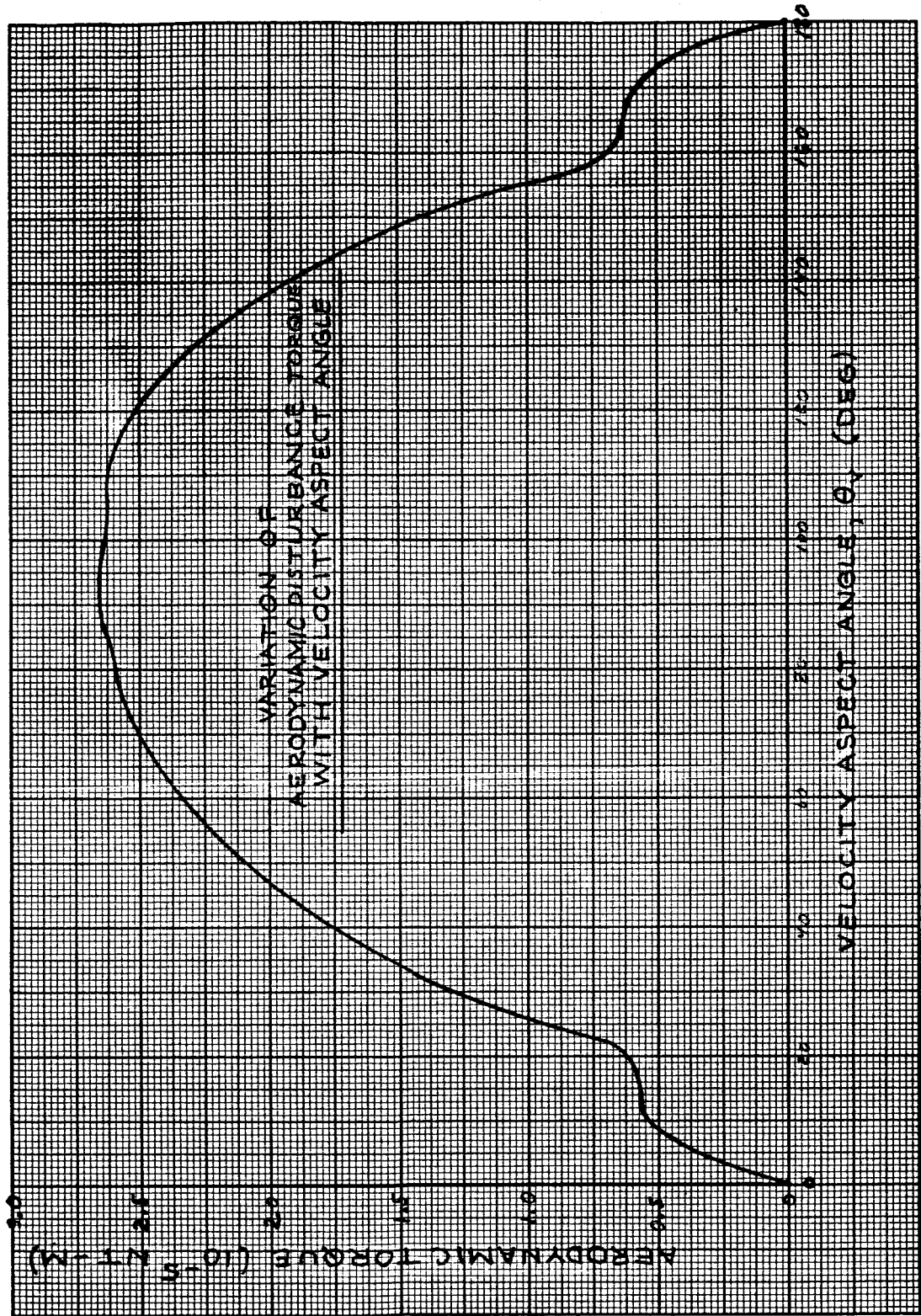


Figure 8 Variation of Aerodynamic Disturbance Torque With Velocity Aspect Angle

## 2.7 Dynamical Conclusions and Recommendations

It is concluded that the spin rate behavior of Ariel II can be readily explained as the result of aerodynamic spin torques exerted on the solar paddles which act as a four-bladed propeller. Because of the elliptical orbit these torques occur only near the perigee condition each orbit. The relatively large spin deceleration experienced at the beginning of the flight developed because the vehicle initially was nearly in alignment with the perigee velocity vector. Subsequent periods of spin acceleration were produced as a consequence of reversals in the relative wind.

It is further concluded that the relatively small attitude wander of the spacecraft's orientation vector is the result of gravity gradient and aerodynamic disturbance torques. A substantial precession rate was calculated for the aerodynamic precession torque, and the maximum gravity gradient torque was shown to be of the same order of magnitude as the aerodynamic torque.

It is recommended that no further effort be expended on the dynamic analysis of Ariel II for the following reasons:

a. The present effort provides an adequate explanation of the spin rate behavior of the satellite. Spin rate is the area of primary interest since it directly involves the operational effectiveness of the experiments aboard the satellite. These experiments rely on satellite spin for their scanning means, and the galactic noise dipole requires a spin rate to retain its form.

b. The attitude information is subject to definite errors which may at times be significant since these data could not be measured directly and had to be entirely derived. A number of assumptions had to be made while developing this attitude information. Therefore it is felt that the quality of the attitude information, while adequate for the qualitative work already performed, is not such as to warrant further effort.

It is recommended that on future spacecraft designs, when operating within the sensible atmosphere of the earth, that careful attention be given to the spin torques which could possibly be developed by unsymmetrical aerodynamic surfaces such as solar paddles, radiators, and other large surfaces.

It is further recommended that attitude and attitude rate sensors be installed on all significant spacecraft, particularly when they are

experimental or developmental in nature. Provisions should be made to either store this attitude information or provide such information on a continual basis so that it can be telemetered back to earth on either a programmed or a command basis.

### 3.0 POWER SYSTEM PERFORMANCE

This section is a presentation of the results obtained from Phase III effort in the analysis of the power system performance of the UK-2/S-52 International Satellite. The Phase III effort is essentially an extension of Phase II wherein the data of Phase I was examined with respect to prelaunch performance data to note and document gross defects and/or anomalous behavior of the power system.

Briefly, the results of Phase II may be summarized by stating that no permanent faults were observed, and with the exception of the following anomalies, the power system performed successfully with respect to the long-life requirements of the UK-2/S-52 satellite. Anomalous behaviors cited were:

1. Unusual variation of telemetered performance parameters and a lapse of telemetry in orbit number 415.
2. Low output power from solar cell array in orbit number 704.

Also a Phase II recommendation was to determine solar cell array degradation as a function of time.

In Phase III the anomalous behaviors noted in Phase II are examined in greater detail to explain the probable cause. Further analysis of Phase I data is made in an attempt to determine the degradation of the battery and the solar cell array.

#### 3.1 Battery Performance

The data available which relates to the battery are performance parameters:

- PP No. 07 - Unregulated Bus (battery terminal voltage)
- PP No. 10 - Battery Current
- PP No. 11 - Battery Temperature

This data has been analyzed to 1) determine degradation of terminal voltage, 2) determine degradation of charge efficiency, and 3) determine if the standby

battery was used. It was concluded in Phase II studies that the standby battery was not employed since the 18 hour interval timer was never activated. The analysis performed herein is aimed at supporting the preliminary conclusion by the presentation of additional evidence.

### 3.1.1 Battery Terminal Voltage

A curve of maximum battery terminal voltage versus battery temperature is shown in Figure 9. The data was obtained from the 200-day graphs of Phase I, and each data point is referenced according to days from launch. Since a favorable power balance existed, the maximum terminal voltage observed corresponds approximately to that of a fully charged battery. Similarly, high battery temperature would occur during daytime as the battery overcharged. (It is interesting to note however, that the variation of battery temperature in a given day-night orbit was in general 4°C or less.) Averaging the data points, two distinct slopes are obtained. The minimum slope corresponds to battery terminal voltages where voltage limiting action by the battery charge and protective circuit occurred. Voltage limiting is accomplished by a reduction in battery charge current and occurs only at cold temperatures due to the characteristic negative temperature coefficient of battery terminal voltage. 16.34 and 16.43 volts are the average voltage limit points at 16°C and -15°C respectively. The 90 mv change in voltage limit point for a 31°C temperature change corresponds with pre-launch data of -3mv/oc stability of the voltage limit electronics. The absolute values appear to be shifted downward approximately 0.1 volt, however this apparent error is only 0.6% and may be attributed to measurement resolutions in pre-launch and post-launch data.

The conclusion drawn from the data of Figure 9 is that no apparent degradation in battery terminal voltage occurred over the 190-days where data is available.

### 3.1.2 Battery Charge Efficiency

In general, the terminal voltage of the battery is not indicative of the battery charge state because of the plateau region in the voltage-ampere hour characteristic of a Ni-Cd cell. Hence there are no exact means of determining the battery charge efficiency in a particular charge-discharge cycle. It follows that the ability to determine degradation in charge efficiency as a function of time is limited.

FIGURE 9

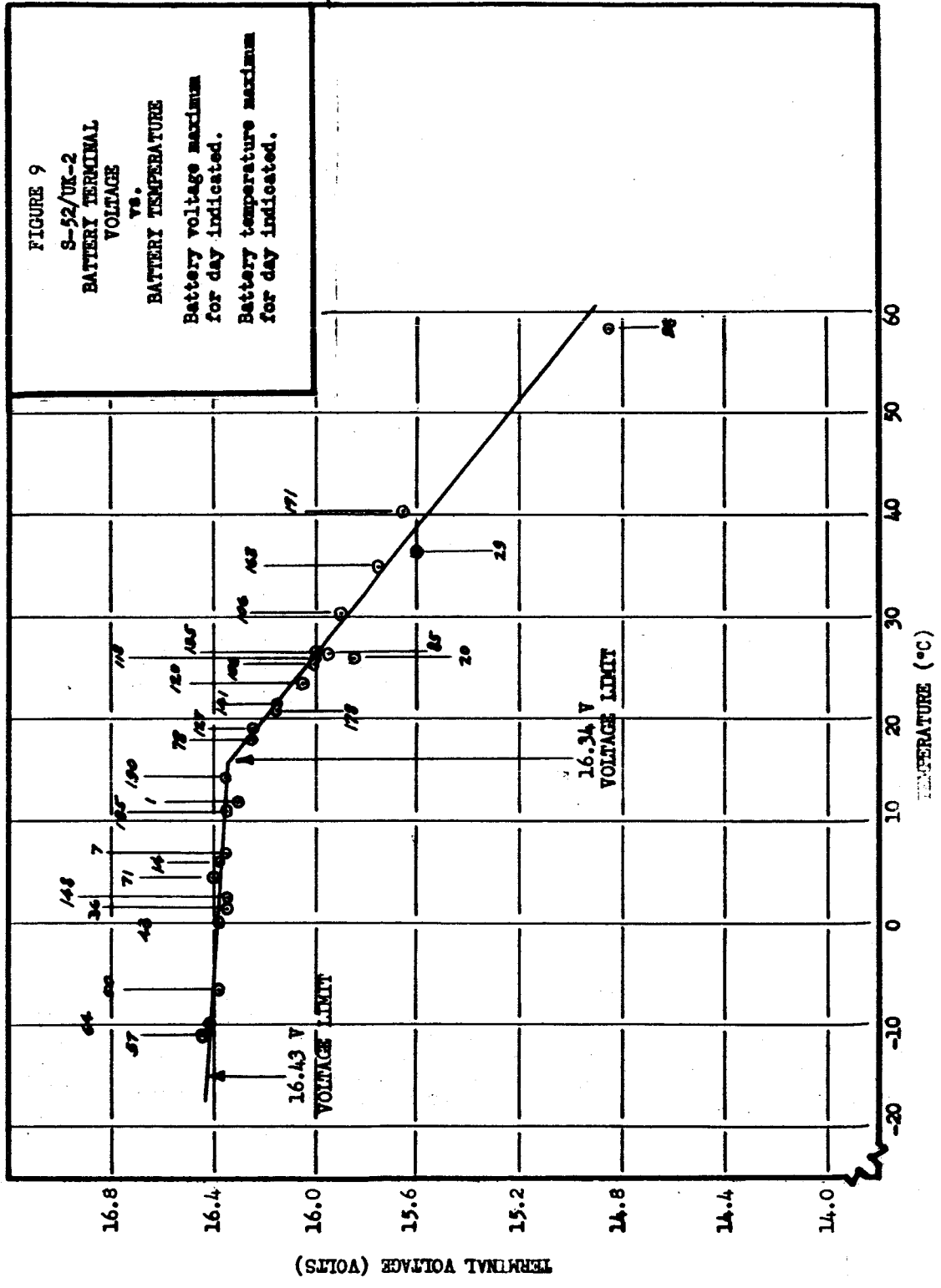
S-52/UK-2  
BATTERY TERMINAL  
VOLTAGE

vs.

BATTERY TEMPERATURE

Battery voltage maximum  
for day indicated.

Battery temperature maximum  
for day indicated.



A characteristic of the Ni-Cd battery does exist whereby terminal voltage can be used as a rough indication of charge state. At cold temperatures, less than approximately 15°C, the terminal voltage rises rapidly above the aforementioned plateau region in the terminal voltage-ampere hour characteristic as the battery approaches the fully charged state. This phenomenon occurs as the battery begins to "over-gas". The over-voltage limiting function of the battery charge and protective unit in the power system was designed to capitalize on this battery voltage phenomenon and thereby reduce charging current to minimize "over-gasing".

Since maximum battery terminal voltage as a function of temperature in Figure 9 showed no unusual variations with time, it was decided to plot a scatter diagram of battery charge time versus days after launch. The "charge time" is defined here as the time required to reach a specified terminal voltage after entering sunlight. Sunlight entrance times were determined from percentage sunlight curves of Phase I, and the charge time to specific voltages determined from the composite orbit graphs, also of Phase I. The data points shown in Figure 10 are labeled with the percent sunlight, battery temperature and aspect angle to enable correlation of similar conditions which affect battery charge time. Correlation of percentage sunlight is important since the discharge ampere-hours in darkness would be equal (assuming consistent load). Battery temperature is important since charge efficiency is related, becoming better at cold temperature. Aspect angle affects the solar array output current as a function of time, when the satellite enters daylight. It is believed that aspect angle is of least importance, and the assumption is made that the effects of solar cell array degradation are negligible since excessive solar current was available shortly after daylight entrance.

Correlation of a few data points at 16.0 volts is shown by straight lines A and B. Line C shows the charge time to 16.35 volts with correlated conditions of line B. Although the data may be interesting, the assumptions that must be made, the limited data available, and the accumulative errors possible in data measurement and reduction shade the results. However, be that as it may, the analysis does not indicate a degradation in battery charge efficiency.



### 3.1.3 Battery Temperature

Maximum and minimum battery temperatures of 59°C and -14.5°C occurred at 98-days and 57-days, respectively, according to the 200-day graphs of Phase I. From the battery cell specification<sup>3</sup> the expected range of ambient operating temperatures, typical of flight conditions, was -5°C to +40°C. Storage temperature and operating temperatures, for design qualification, were specified to be -30°C  $\pm$ 2°C to +60°C  $\pm$ 2°C and -15°C  $\pm$ 2°C to 50°C  $\pm$ 2°C, respectively. Although anticipated ambient temperatures were exceeded, the specified operating temperatures were exceeded only at hot temperature. The 59°C measurement of battery temperature may be subject to large error since the range of the temperature measurement was bounded at 60°C. The fact that the battery was operated (at least continually charged at 500 Ma. since 100% sunlight at the time) well beyond the specified operating temperature of 50°C with apparently no damage is a creditable note to the quality of the Ni-Cd battery cells.

In further regard to battery temperature, a maximum temperature rise of 23.3°C above lower shelf temperature was predicted<sup>4</sup> for continual overcharge (7.40 watts dissipation). In the period of 96 to 100-days, where 100% sunlight existed and the battery was dissipating 7.45 watts due to continuous overcharge, the battery temperature rise above lower shelf temperature was approximately 20°C. Although battery temperature sensing for the purpose of limiting charge current was originally planned for the battery charge and protective circuit, it was not used in the flight satellite since analyses of lower shelf temperature and battery temperature rise showed no need for temperature limiting by reduction of charge current. It is now believed that temperature sensing should have been included to help prevent excessive operating temperatures.

### 3.1.4 Standby Battery

The minimum unregulated bus voltage observed, from the 200-day graphs, was 13.75 volts at day 135. This fact, coupled with the fact that an 18 hour "transmitter off" period which follows an undervoltage condition was not observed, indicates that the standby battery was not employed. To further support this conclusion is the consistent behavior of battery terminal voltage versus battery temperature shown in Figure 9. (Battery temperature, PP No. 11 associated only with launch-time "on-bus" battery.) Furthermore, maximum battery

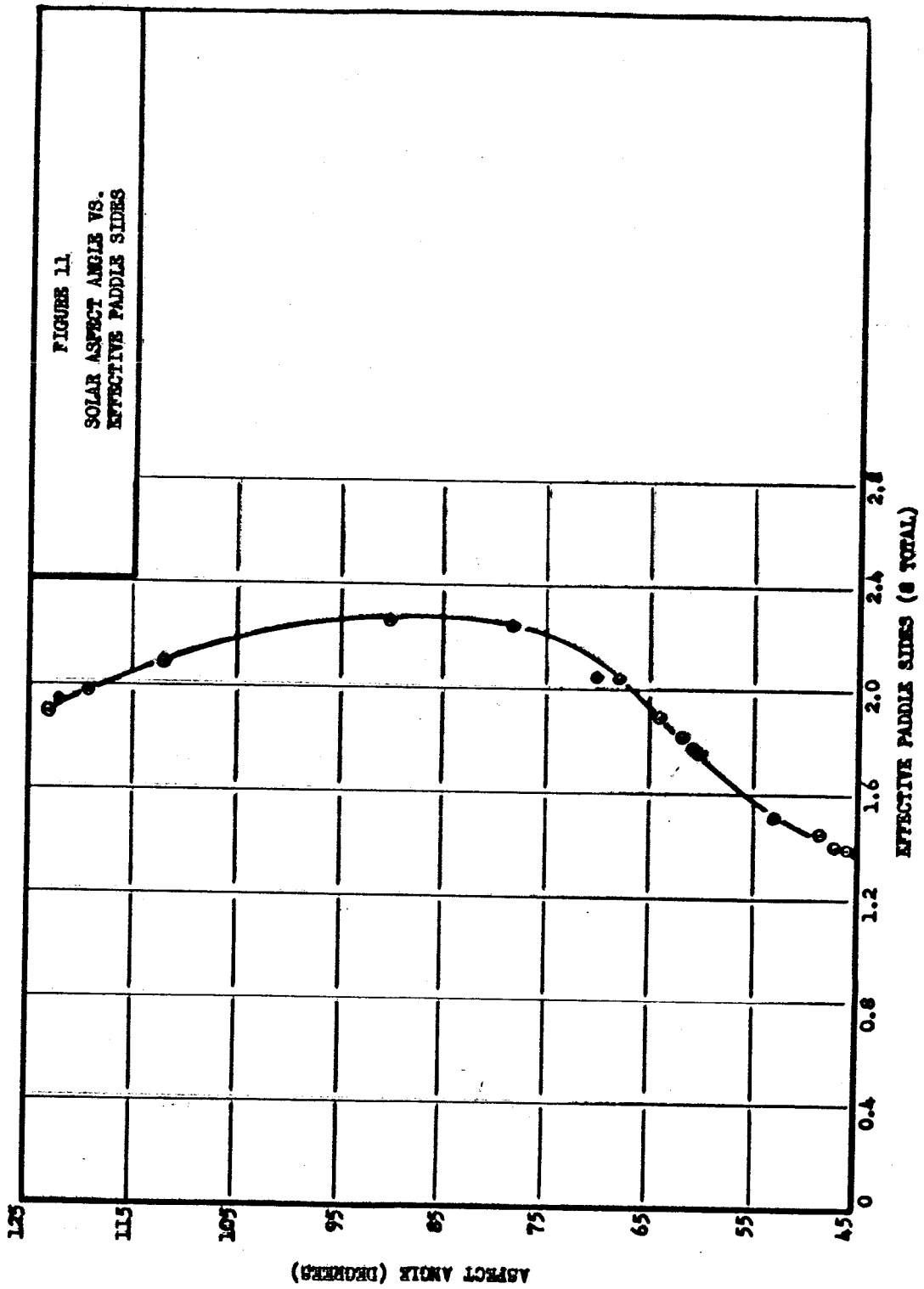
temperature as related to maximum lower shelf temperature ranged from 0 to 5°C higher except for three periods of high percentage sunlight. In these periods (22 to 31, 95 to 101 and 167 to 169 days) battery temperature rise above lower shelf was significantly higher, 10 to 20°C, thus indicating the launch time "on-bus" battery was still on the bus.

### 3.2 Solar Paddles Performance

The current output of the solar cell array, unlike battery terminal voltage for example, fluctuates widely within a given orbit. The spin modulation and the rapid temperature changes of the solar paddles after sunlight entrance are primarily the factors affecting solar current variations within a single sunlight period. Over a period of days the changing aspect angle affects the solar paddles output current. These orbital and day-to-day influences on solar paddles current cause considerable difficulty in any analysis of solar cell array degradation.

One method employed to analyze the solar cell array performance was to determine, from the composite orbit graphs, unregulated bus voltage (PPO7), paddle No. 4 temperature (PP12), and percent sunlight data corresponding in time with the maximum observed solar current (PPO9) for the same orbit. The aspect angle was also determined by reference to the curve of aspect angle versus days from launch which was calculated in Phase II. Using the curve of Figure 11, reproduced from data presented in reference 5, the effective paddle sides for particular aspect angles were determined, and all observed maximum solar currents were increased by the ratio of  $\left[ 2.27 \text{ (maximum effective paddle sides)} \right] : \left[ \text{effective paddle sides for the given aspect angle} \right]$ .

A scatter diagram of the normalized solar current versus days from launch is shown in Figure 12. Data points are labeled with the observed paddle temperature and unregulated bus voltage. Correlation of data having approximately equivalent conditions should provide an indication of solar paddle degradation. It is observed that at days 36 (orbit 508) and 148 (orbit 2109) approximately equal conditions of bus voltage and solar paddles temperature exist. Also at days 1 (orbit 10) and days 141 (orbit 2010) equivalent conditions are noted. The apparent degradation of the solar cell array is then computed as follows:



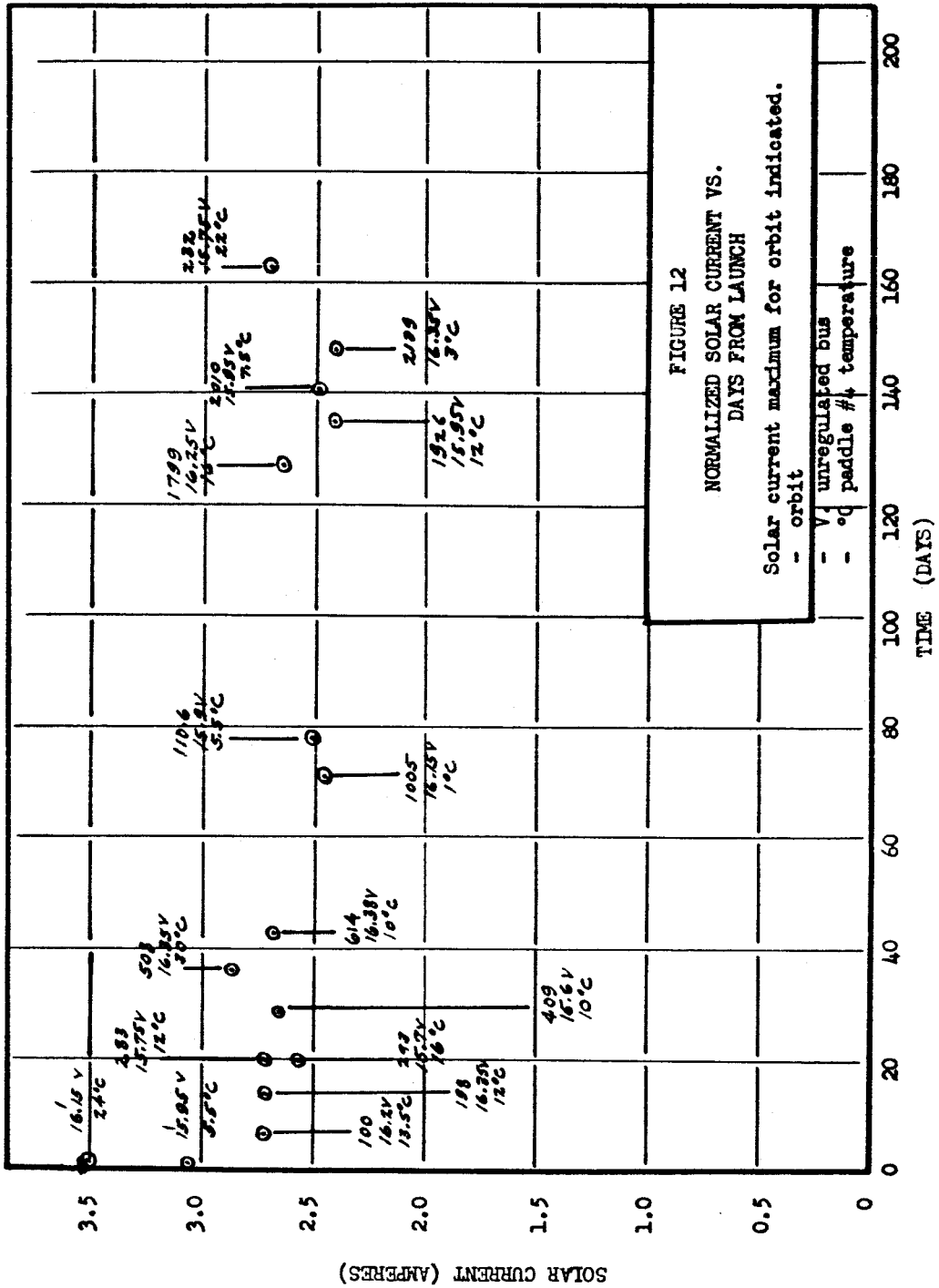


FIGURE 12  
 NORMALIZED SOLAR CURRENT VS.  
 DAYS FROM LAUNCH  
 Solar current maximum for orbit indicated.

- V unregulated bus  
 - °C paddle #4 temperature

| <u>Orbit</u> | <u>Maximum Current Observed (Normalized)</u> |
|--------------|--|
| 10           | 3.06 amps                                    |
| 2010         | 2.48 amps                                    |

$$\frac{i_{10} - i_{2010}}{i_{10}} (100\%) = 19\%$$

Average Degradation = 0.0095%/orbit  
(= 0.136%/day)

| <u>Orbit</u> | <u>Maximum Current Observed (Normalized)</u> |
|--------------|--|
| 508          | 2.86 amps                                    |
| 2109         | 2.41 amps                                    |

$$\frac{i_{508} - i_{2109}}{i_{508}} (100\%) = 15.7\%$$

Average Degradation = 0.0098%/orbit  
(= 0.14%/day)

The solar paddles were subject to large temperature variations, typically in excess of 50°C, for orbits of approximately 100% sunlight. The rate of change of temperature as a function of time was approximately 2°C/Min. and it is expected that relatively large temperature gradients would exist on the paddles. Such gradients would affect the current output of the active series strings of solar cells (4 paddles, 4 strings per paddle, 48 series sub-modules per string, and 7 parallel solar cells per submodule) because of the temperature dependence of solar cell output voltage (2.3 mv/°C per cell). The maximum solar currents observed and plotted in the scatter diagram of Figure 12 occur during the high rate of change in paddle temperature and therefore are subject to a number of unknowns.

In reference 5 it was predicted, assuming a probably worst case condition of variables influencing the preservation of adequate electrical power, that the N-on-P paddles would provide a comfortable power balance for at least 150-days. The anticipated hard particle radiation effects of energetic electrons was predicted to be as follows within a period of 150-days:

| Elapsed Time<br>Following Launch | Radiation<br>Dosage              | Current from<br>Unradiated Paddle (-) | Current Degradation of Radiated Paddle |
|----------------------------------|----------------------------------|---------------------------------------|--|
| (Days)                           | (MEV Electrons/cm <sup>2</sup> ) | %*                                    | %**                                    |
| 0                                | 0                                | 100                                   | 100                                    |
| 150                              | 1.5 x 10 <sup>15</sup>           | 65                                    | 77                                     |
|                                  |                                  | Av. = 0.23%<br>per day                | Av. = 0.15%<br>per day                 |

\*NASA-GSFC "Specification for Determining Relative 1 MEV Electron Radiation Damage for Silicon Solar Cells", Spec. No. 63-106, Oct. 31, 1962.

\*\*F. M. Smits, W. Rosenzweig, W. L. Brown, "Report of Solar Cell Work at Bell Telephone Laboratories" dated 27 February 1962, Proceedings of the Solar Working Group Conference, Vol. I, Radiation Damage to Semiconductor Solar Devices.

The degradation above was the effect of radiation on short circuit current. Assuming that this degradation in output current may be extrapolated toward the open-circuit condition, the results of the degradation analysis of 0.14% per day, on the average, relates fairly well to predicted degradation due to hard particle radiation.

The results of the analysis performed for solar cell degradation are not as conclusive as desirable due to the limited amount of data available from Phase I which fits into the correlation scheme. It appears, however, from available data, that solar cell array output current decreased due to anticipated causes, i.e., discoloration, radiation damage and micrometeorite erosion, and that no major malfunction was encountered with the solar paddles.

### 3.3 Regulators

The low voltage power supply system is shown in the simplified diagram of Figure 13. This diagram is presented to review the interrelationship of the power supply functional blocks. Also shown are a few of the power supply loads which relate to a later discussion, section 3.4, of the anomalous behavior of performance parameters in orbit 415.

#### 3.3.1 Battery Charge and Protection Circuit

The battery charge and protection circuit, which includes the shunt regulator employed for dumping excess solar paddles current, performed the

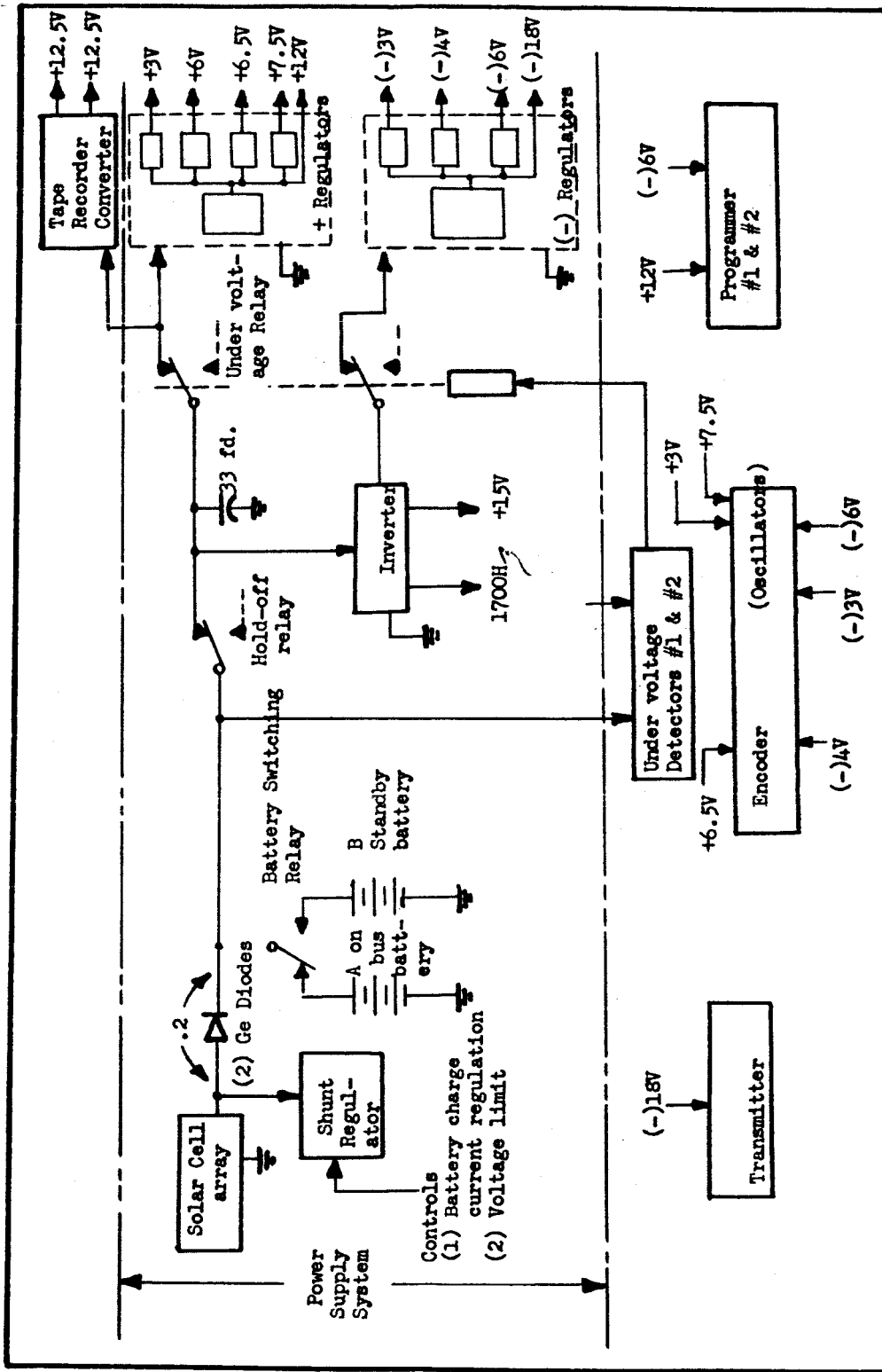


FIGURE 13  
SIMPLIFIED POWER SUPPLY SYSTEM  
DIAGRAM

functions of battery terminal voltage limiting (reference section 3.1.1) and battery charge current regulation as predicted by pre-launch data. It is appropriate to note in regard to Phase I data that the battery charge current decreased below the 500 Ma.  $\pm 2\%$  level at cold temperatures due to two reasons. First, when voltage limiting occurs at cold battery temperatures, the charge current is reduced to a value required to maintain the battery terminal voltage at the limit point. Second, the charge current is reduced at cold temperatures to compensate for increased battery charge efficiency. Reduction of charge current is a function of the temperature of the charge current regulator electronics, and a linear decrease from 500 Ma. to approximately 385 Ma. is obtained in going from  $20^{\circ}\text{C}$  to  $-15^{\circ}\text{C}$ . From  $20^{\circ}\text{C}$  to  $50^{\circ}\text{C}$  the charge current is regulated at 500 Ma.  $\pm 2\%$ . The characteristics of the charge current regulator are discussed here to explain the excursions of this parameter which were reported in Phase II as a possible anomaly.

### 3.3.2 Plus and Minus Regulators

The performance parameters which relate to the regulated power supplies are +15 volts (PP No. 04), G. N. Reel +12V (PP No. 08) and battery current, discharge (PP No. 10). As shown in Figure 13, the +15V is obtained via the inverter, while the +12V is obtained directly from the unregulated bus. The regulation of these supplies was within the  $\pm 0.1$  volt limits predicted by Pre-launch data (within measurement resolutions) except for the anomalous period in orbit 415. The performance of other regulators (plus 3, 6, 6.5, 7.5V and minus 3, 4, 6, 18V) are not directly known; however, the behavior of battery discharge current (regulators and associated loads) was not abnormal and the performance of the satellite electronics in general attest to the satisfactory performance of the unmonitored regulated voltages.

## 3.4 Power System Anomalies

### 3.4.1 Orbit 415 Anomaly

The anomaly in orbit 415, reported in Phase II and illustrated by plots of performance parameters from time 21/55/00 to 22/07/00, may be described as an unexpected variation in magnitudes of parameters for approximately a 4-minute period and a lapse in telemetry for approximately 3-minutes. Furthermore, the magnitude changes occurred in discrete steps before loss of telemetry, and after the 7-minute period in question, performance parameters returned to normal.

Assuming a power system fault responsible for the anomaly, hypotheses are developed which can explain the observed phenomenon. The following factors are considered:

1. The fault occurred in a sunlight period during the 29th day after launch. From the 200-day graph of percent sunlight (Phase I) it is observed that 100% sunlight existed from approximately day 23 to day 30. At day 29 the highest lower shelf temperature (15°C) was experienced since launch. Temperature excursions of the lower shelf were a maximum and minimum of 15°C and -7°C respectively for the first 29 days.

2. An undervoltage detection did not occur. The undervoltage detection circuit senses unregulated bus voltage (Figure 3.3-1) and will not be activated by loss of a regulated voltage. The analysis in section 3.1.3 showed that no undervoltage condition or battery switching occurred.

3. Telemetered performance parameter Nos. 04, 05 and 07 through 12 inclusive decreased in magnitude during the 4-minute period of abnormal behavior. This relative change corresponds to an increase in frequency of the telemetry oscillators. PP No. 06 increased in magnitude which also corresponds to an increase in frequency of the telemetry oscillator. The magnitudes of parameters before and after the anomaly as well as the maximum change during the 4-minute period of variation are listed in Table 3.4-1. Also shown are the approximate changes in frequency of the oscillator which were determined from the calibration curves presented in Phase I, Volume I report.

A significant observation in Table 3.4-1 is that all analog oscillators, for the performance parameters plotted in Phase II, increased in frequency during the anomaly. The variables which affect oscillator frequency, external to the oscillator circuit, are the 7.5V  $\pm$ .25% and (-) 3V  $\pm$ .25% power supplies, input analog signal voltage and magnetic fields. The analog oscillator inputs are derived from sensing circuits which are energized from different regulators. Sensing circuits for +15V, +12V and unregulated bus voltage are passive circuits; all other circuits are active. Table 3.4-2 is a list of performance parameter sensing circuits and the associated power supply source.

Referring to the power supply system diagram of Figure 13, it is seen that a malfunction in the 6.5 volt regulator, or the 12 volt regulator

| FP No. | Description               | PP Magnitude   |               | PP Magnitude Change | 4-Minute Variation                  |                  |
|--------|---------------------------|----------------|---------------|---------------------|-------------------------------------|------------------|
|        |                           | Before Anomaly | After Anomaly |                     | Approx. Oscillator Frequency Change | K H <sub>Z</sub> |
| 04     | +15 Volts                 | 15.1V          | 15.1V         | (-) 0.4V            | 0.2                                 | 3                |
| 05     | Tape Recorder Temperature | 10.2°C         | 10.2°C        | (-) 8.2°C           | 0.6                                 | 5.5              |
| 06     | Dump Current*             | 0.4a           | 0.52a         | + 0.12a             | 0.4                                 | 5.5              |
| 07     | Unregulated Bus           | 15.57V         | 15.61V        | (-) 0.17V           | 0.5                                 | 7                |
| 08     | +12 Volts                 | 12.03V         | 12.03V        | (-) 0.73V           | 0.6                                 | 5                |
| 09     | Solar Current*            | 1.32a          | 1.5a          | (-) 0.08a           | 0.2                                 | 2                |
| 010    | Battery Current           | 0.51a          | 0.51a         | (-) 0.07a           | 0.6                                 | 6                |
| 011    | Battery Temperature       | 33.7°C         | 33°C          | (-) 5.2°C           | 0.5                                 | 5.5              |
| 012    | Paddle #4 Temperature     | 1°C            | 3°C           | (-) 11°C            | 0.4                                 | 3                |

\*Average Value

Table 3.4-1  
PERFORMANCE PARAMETER BEHAVIOR - ORBIT 415

| PP No. | Description               | Sensing Circuit Power Supply            |
|--------|---------------------------|---|
| 04     | +15 Volts                 | (Passive Circuit)                       |
| 05     | Tape Recorder Temperature | +6.5V Regulator                         |
| 06     | Dump Current              | 15V p-p, 1700 H <sub>z</sub> (Inverter) |
| 07     | Unregulated Bus Voltage   | (Passive Circuit)                       |
| 08     | +12 Volts                 | (Passive Circuit)                       |
| 09     | Solar Current             | 15V p-p, 1700 H <sub>z</sub> (Inverter) |
| 010    | Battery Current           | 15V p-p, 1700 H <sub>z</sub> (Inverter) |
| 011    | Battery Temperature       | +6.5V Regulator                         |
| 012    | Paddle #4 Temperature     | +6.5V Regulator                         |

Table 3.4-2

PP SENSING CIRCUIT POWER SUPPLIES

which supplies the 6.5 volt regulator input, would not affect PP Nos. 04, 06, 07, 09 or 10 at the sensing circuit. Likewise, a malfunction in the inverter would not affect PP Nos. 05, 07, 08, 11 or 12. Unregulated voltage is the parameter which could affect all PP sensing circuits if a decrease below the preset undervoltage level occurred. Since undervoltage did not occur it is concluded that the reason for abnormal variation of PP magnitudes was not due solely to variation in analog oscillator input signals. The reason for variation of the analog oscillators is thus narrowed to the possibilities of 1) a change in the +7.5 and/or (-) 3V regulated power supply voltages and 2) an external magnetic field.

Based on information from GSFC, data is not available for the 3-minutes in the anomalous period due to a "quiet" satellite transmitter. A loss of regulated (-) 18 volts (transmitter power supply) from the inverter would account for a break in the telemetry link. It is reasonable to assume that a malfunction occurred in the power inverter which was manifested by intermittent oscillation for a 4-minute period and no oscillation for a 3-minute period. The transition from normal oscillation to inoperative could occur with varying degrees of intermittent operation, thus accounting for the apparent step changes in performance parameters. The effect of the intermittent inverter operation on the (-) 3 volt regulator, to account for an increasing frequency from the analog oscillator, would be an increase in magnitude (more negative). Although intuition would lead to a predicted decreasing -3V (more positive) for a reduced regulator input voltage, it is possible to obtain the opposite effect. A mathematical analysis of any given regulator design to predict the actual change in output voltage as a function of input voltage (particularly when input voltage exceeds design limits) is complex. A mathematical analysis or electrical test of regulator circuits is beyond the scope of the Phase III task. Hence in postulating an inverter malfunction it must be assumed that the -3V power supply actually increased in magnitude by approximately 5 to 10%.

Since the (-) 18 volt regulator, fed from the inverter, is the input to the (-) 3 volt regulator it would be reasonable to postulate that a (-) 18 volt regulator malfunction occurred rather than an inverter malfunction. It is observed from table 3.4-1 that unregulated bus voltage increased from 15.57 to 15.61 volts in the 7-minute period. Since the anomaly occurred at the end of a 100% sunlight period it is reasonable to assume that the battery was fully charged. The 15.57 volts terminal voltage before the anomaly is reasonable for the battery temperature of 33°C. After the anomaly, unregulated bus voltage was 15.61 volts. As previously discussed in section 3.1.1, terminal voltage is not in general indicative of battery charge state, however, even the 40 mv increase in terminal voltage experienced in the anomalous period can be an indication that a large increase in charge current occurred. Since the battery charge-current regulator is dependent on 1700 H<sub>Z</sub> from the inverter for regulation of charge current at 500 Ma., loss of the 1700 H<sub>Z</sub> would result in no dump current. Solar paddle current minus load current would then be directed to the battery.

In conclusion, probable cause of the anomaly, if a power system fault, is a malfunction of the inverter. Cause of the inverter malfunction might be explained by a cold-solder connection which "acted-up" due to several cycles in lower shelf temperature between approximately  $-7^{\circ}\text{C}$  and  $15^{\circ}\text{C}$ . The anomaly occurred at a 100% sunlight period where temperatures in the satellite were highest experienced since launch. Whatever the type of failure, it is evident that a self-healing action occurred in a very short time period and it is more reasonable to assume a faulty connection than a faulty component.

#### Magnetic Fields

Although the probably cause of the orbit 415 anomaly was an inverter malfunction, it should be pointed out that encountering a strong external magnetic field could also account for the observed phenomena of frequency shifts in the telemetry oscillators. Just as the external magnetic field would affect the magnetic cores of the analog oscillators, it is also reasonable to expect such a disturbance on the inverter could interrupt oscillation. The presence of a strong external magnetic field reasonably explains the observed phenomenon, but the source of such a magnetic field for a 7-minute interval is not easily explained.

#### 3.4.2 Orbit 704 Anomaly

The anomaly in orbit 704, reported in Phase II, was an apparent deficiency in the power available from the solar paddles for a time of approximately 15-minutes prior to exit from sunlight. At times 32.5 and 37.5 minutes on the composite orbit graphs for orbit 704, the available (solar current x unregulated bus voltage) product, or available power, was less than the pre-launch predicted minimum of 14 watts. Also, earlier and later orbits did not show less than 14 watts available power, prior to exit from sunlight, as prematurely as encountered in orbit 704.

It was noted, upon examining the composite orbit graph for base orbit graph for base orbit 704, that a discrepancy exists in plotted data for PP No. 09, solar current. The data expanded for a 5-minute period around 17.5 minutes ( data for orbit 710) does not agree with the maximum and minimum solar current data points plotted at that time. Furthermore, the sum of dump current and battery charge current were equal to solar current, indicating zero load current.

The data in question was checked on the data reduction work sheets of Phase I for possible error, and an error was discovered in the plot of maximum and minimum solar current data points in the time interval of 0 to 37.5 minutes inclusive. A scale shift of 0.4 amperes occurred in plotting data such that 1.0 amperes shown on the ordinate is actually 1.4 amperes. Minimum available power at 37.5 minutes is thus (0.9 amps x 16.37 volts) or 14.7 watts. The data points from 52.5 to 97.5 minutes were plotted in correct relationship to the ordinate scale.

It is concluded that the apparent anomaly reported in Phase II was actually not an anomaly, but instead an error in solar current data plotted for base orbit 704.

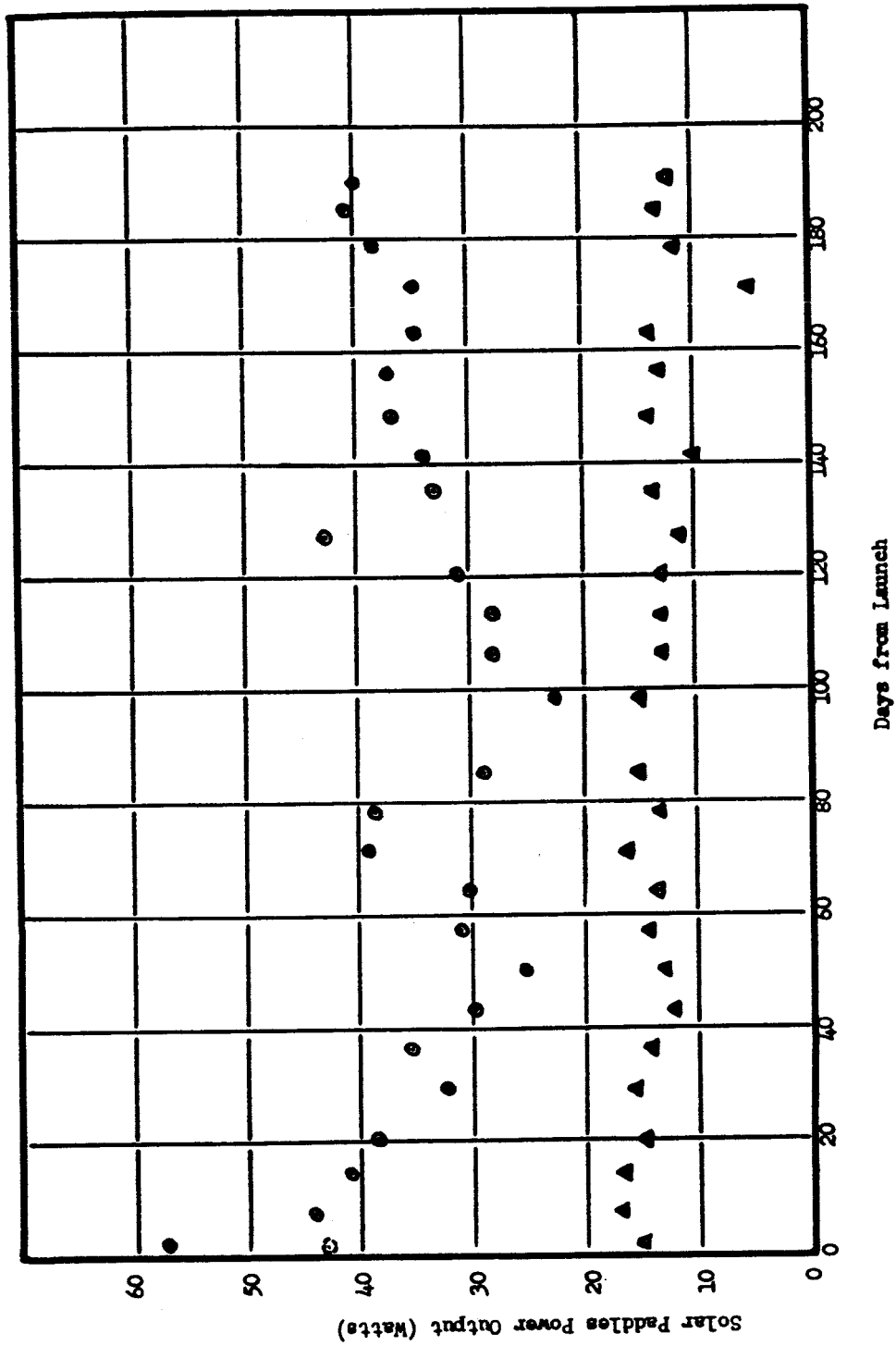
### 3.4.3 Initial Power Loss Anomaly

Initial review of telemetered data by GSFC had indicated the possibility that solar paddle power dropped markedly within the first few days from launch. It had been recognized that this rapid assessment of the data had not produced results in which high confidence could be placed. Perhaps the major reason for lack of confidence was the high amplitude of spin modulation which characterized solar paddle output for certain aspect angles. The initial data review consisted of plotting results from small data samples so that only a peak or valley of the modulated power output might have been examined for a particular point. Nevertheless, the possibility of an early power loss was examined further.

Figure 14 illustrates the upper and lower bounds for power output versus days from launch. The circular points were determined by computing the power that would result from the maximum unregulated voltage and the maximum solar current (pp 07 and pp 09) for the given day. A simultaneous occurrence of these maxima is extremely doubtful, of course, but this result represents an upper bound. The triangular points were computed in a complementary fashion by assuming simultaneous occurrence of minima. It may be noted from Figure 14 that except for one upper bound point early in the history, the limits are well behaved and that the upper bound follows to some extent the variation in solar aspect angle, as might be expected.

The one upper-bound point cited was rechecked in the original GSFC data print outs to see whether or not there had been an error in data reduction.

FIGURE 1A  
 SOLAR PADDLE POWER VERSUS DAYS FROM LAUNCH



Although data reduction had been without error two facts can be noted which put the point in question. First the current value 3.5 + amps corresponding to this point was in a very nonlinear region of the oscillator which responded to solar current (see Figure 20, of reference 1, Volume I). Moreover this value is on a very steep slope of the oscillator operating curve and is near the saturation level. These considerations seriously degrade the accuracy of measurement for these values. Secondly, the data points immediately adjacent to the point in question are very much lower, namely 1.9 amps and 2.2 amps. Also the maximum current for the next day was only 2.7 amps. If 2.7 amps is used instead of 3.5 the point shown dotted in Figure 14 results. The conclusion reached in respect to this area of concern is that no serious power drop was experienced in the early orbital period and that variations in the power upper bound as shown in Figure 14 can be attributed to solar aspect angle.

### 3.5 Power System Conclusions

The several conclusions which have been drawn in this section are summarized below in order of their occurrence in the foregoing pages.

1. Battery Terminal Voltage. The pre-launch, observed  $-3\text{mv}/^\circ\text{C}$  stability of the voltage-limiting electronics was borne out in the actual performance record.

2. Battery Charge Efficiency. Although difficult to assess, a qualified conclusion is drawn that no degradation in battery charge efficiency took place during the 190-days studied.

3. Battery Temperature. Battery temperature exceeded specification levels by at least  $10^\circ\text{C}$  and possibly more; however, the batteries apparently suffered no degradation during this operation. It is now believed that temperature rise limiting through reduction of charge current as a function of battery temperature should have been included in the control circuits.

4. The standby battery was not employed.

5. Solar Paddle Performance. Average solar paddle degradation was computed to be 0.14% per day which correlates fairly well to anticipated degradation due to hard particle radiation. It should be noted that numerical results in this calculation are based on a small data sample. There were no major malfunctions.

6. Regulators. The +12 and +15 volt regulators functioned within tolerance, as far as measurement resolutions permit determination. Generally satisfactory performance of the spacecraft electronics indicates satisfactory regulation in the unmonitored supplies.

7. The Orbit 415 Anomaly. The most probable cause, if the power system is at fault, is the inverter. A cold solder connection which became intermittent because of mechanical stress imposed by higher than usual temperatures is a hypothesis for a detailed cause within the inverter.

8. The Orbit 704 Anomaly. This previously reported deficiency proved to be a false one based upon incorrectly plotting Phase I data in this orbit.

## REFERENCES

1. Phase I Report, Ariel II Engineering Data Analysis, 23 June 1965.
2. Phase II Report, Ariel II Engineering Data Analysis, 8 September 1965, (2 Volumes).
3. "Battery Cell Specification for International Satellite UK-2/S-52" (Westinghouse PDS 21180) May 21, 1962.
4. "Statement of Thermal Requirements for Westinghouse-Furnished Equipment on the UK-2/S-52 International Satellite" (UK-2/S-52 Technical Memorandum No. 2) July 3, 1962.
5. "Revised Electrical Load Analysis for UK-2/S-52 International Satellite Electrical Power Supply" (UK-2/S-52 Technical Memorandum No. 6) December 6, 1962.